



UPPSALA
UNIVERSITET

*Digital Comprehensive Summaries of Uppsala Dissertations
from the Faculty of Science and Technology 1670*

Diamond Devices Based on Valley Polarization

NATTAKARN SUNTORNWIPAT



ACTA
UNIVERSITATIS
UPSALIENSIS
UPPSALA
2018

ISSN 1651-6214
ISBN 978-91-513-0335-2
urn:nbn:se:uu:diva-348551

Dissertation presented at Uppsala University to be publicly examined in Siegbahnsalen, Ångströmlaboratoriet, Lägerhyddsvägen 1, Uppsala, Friday, 8 June 2018 at 13:15 for the degree of Doctor of Philosophy. The examination will be conducted in English. Faculty examiner: Hitoshi Umezawa (AIST, Osaka, Japan).

Abstract

Suntornwipat, N. 2018. Diamond Devices Based on Valley Polarization. *Digital Comprehensive Summaries of Uppsala Dissertations from the Faculty of Science and Technology* 1670. 88 pp. Uppsala: Acta Universitatis Upsaliensis. ISBN 978-91-513-0335-2.

Diamond is a wide bandgap semiconductor with extreme properties such as high thermal conductivity, high breakdown field, high carrier mobilities and chemical inertness. These properties together with the possibility to synthesize high purity Single-Crystalline (SC) diamond by Chemical Vapor Deposition (CVD), make it a very interesting material and a candidate for use in power electronics and in hazardous environments. The low impurity concentration achieved when fabricating diamond by CVD allows for a detailed study of the intrinsic electronic properties.

Diamond has six equivalent conduction band valleys oriented along the {100} axes with a uniquely low scattering rate between them. At low temperatures, the intervalley phonon scattering rate in diamond becomes negligible, which leads to a stable valley polarization state. We have observed non-equilibrium valley populations (valley-polarized electron ensembles), which in turn have been found to result in a Negative Differential Mobility (NDM).

NDM is commonly only observed in direct bandgap materials such as GaAs, InP and CdTe but our group has also observed NDM in diamond at a temperature range of 100 to 150 K. The occurrence of this phenomenon can be explained by electron repopulation, which is the scattering of electrons between different valleys. If NDM is pronounced enough, electric current instabilities build up and give rise to oscillations. By exploiting this phenomenon, a Transferred-Electron Oscillator (TEO) can be constructed for microwave applications.

Further investigations into the valley-polarized electrons seen in diamond could bring it forward as an alternative material for use in electronic devices. This use, called valleytronics, is similar to spintronics but instead of using the electron spin, the polarization in the conduction band valleys is used to transfer information. Digital electronic circuits use the presence or absence of charge to encode information which relies on a rapid redistribution of mobile charge carriers. This requires energy which results in losses and thus sets a theoretical limit to the maximum switching frequency. This is one of the main issues of electronic devices and can be mitigated by using alternative technologies such as spintronics or valleytronics.

In order to get a better understanding of the electron valley repopulation effects, the focus of this doctoral thesis is the study of electron charge transport in SC-CVD diamond at low temperatures. The thesis also aims at using valley-polarized states as a foundation for the creation of electronic devices such as TEOs or valley-transistors, out of diamond.

Keywords: CVD diamond, valleytronics, Negative Differential Mobility, NDM, electron polarization, Time-of-Flight, magnetotransport, carrier transport, drift velocity, valley-transistor, Transferred-Electron Oscillator, TEO, TED, Gunn diode

Nattakarn Suntornwipat, Department of Engineering Sciences, Electricity, Box 534, Uppsala University, SE-75121 Uppsala, Sweden.

© Nattakarn Suntornwipat 2018

ISSN 1651-6214

ISBN 978-91-513-0335-2

urn:nbn:se:uu:diva-348551 (<http://urn.kb.se/resolve?urn=urn:nbn:se:uu:diva-348551>)

*To my lovely daughter
Evelyn
and my wonderful families
Suntornwipat & Hägglund*

List of papers

This thesis is based on the following papers, which are referred to in the text by their Roman numerals:

- I **N. Suntornwipat**, M. Gabrysch, S. Majdi, D. J. Twitchen and J. Isberg, *Magnetotransport study of valley-polarized electrons in synthetic diamond*, Physical Review B **94**, 035408 (2016).
- II **N. Suntornwipat**, S. Majdi, M. Gabrysch and J. Isberg, *Investigation of transferred-electron oscillations in diamond*, Applied Physics Letters **108**, 212104 (2016).
- III S. Majdi, M. Gabrysch, K. K. Kovi, **N. Suntornwipat**, I. Friel, and J. Isberg, *Low temperature conduction-band transport in diamond*, Applied Physics Letters **109**, 162106 (2016).
- IV J. Hammersberg, S. Majdi, K. K. Kovi, **N. Suntornwipat**, M. Gabrysch, D. J. Twitchen and J. Isberg, *Stability of polarized states for diamond valleytronics*, Applied Physics Letters **104**, 232105 (2014).
- V K. K. Kovi, **N. Suntornwipat**, S. Majdi, M. Gabrysch, J. Hammersberg and J. Isberg, *Charge Transport Phenomena Unique to Diamond*, Mater. Res. Soc. Symp. Proc. **1591** (2014).
- VI **N. Suntornwipat**, S. Majdi, M. Gabrysch, K. K. Kovi, I. Friel and J. Isberg, *Electrostatic control of valley pseudospin in dual-gate diamond transistors*, under revision by Nature Materials.
- VII **N. Suntornwipat**, S. Majdi, M. Gabrysch and J. Isberg, *Transferred-electron oscillators based on diamond*, manuscript.

Reprints were made with permission from the respective publishers.

The author has contributed to the following papers not included in this thesis:

- VIII K. K. Kovi, S. Majdi, M. Gabrysch, **N. Suntornwipat** and J. Isberg, *Surface Passivation of High-k Dielectric Materials on Diamond Thin Films*, ECS Transactions **69** (5), 61-65 (2015).

Contents

1. Introduction.....	11
1.1. Diamond.....	12
1.2. Outline.....	13
2. Electron transport in diamond.....	15
2.1. Band structure	15
2.2. Scattering.....	18
2.2.1. Intravalley scattering	19
2.2.2. Intervalley scattering	20
2.3. Velocity and mobility.....	20
2.3.1. Isotropic case	21
2.3.2. Anisotropic case.....	22
2.4. Charge transport equations.....	23
2.4.1. Fundamental transport equations.....	24
2.4.2. Electron generation and recombination rate	25
3. Drift velocity in diamond.....	27
3.1. At temperatures above 200 K.....	28
3.2. At temperatures between 100 and 200 K	28
3.3. At temperatures below 100 K.....	30
4. Transferred-Electron Oscillators.....	33
4.1. Valley repopulation	33
4.1.1. Negative Differential Mobility	34
4.2. Transferred electron oscillations	35
4.2.1. Simulation.....	35
4.2.2. Experiment.....	41

4.3. Summary	44
5. Valleytronics	45
5.1. Valley-polarized electrons.....	45
5.2. Polarization stability.....	46
5.2.1. Experiment.....	47
5.2.2. Simulation.....	48
5.2.3. Results	49
5.3. Conduction band transport	50
5.3.1. Experiment.....	50
5.3.2. Simulation.....	51
5.3.3. Results	51
5.4. Magnetotransport	53
5.4.1. Experiment.....	54
5.4.2. Simulation.....	54
5.4.3. Results	55
5.5. Valley-transistor	56
5.5.1. Simulation.....	57
5.5.2. Experiment.....	60
5.6. Summary	62
6. Conclusion	63
7. Summary of papers	65
8. Suggestions for future work.....	69
Acknowledgement	71
Summary in Swedish	73
Appendix – Repopulation model evaluation.....	77
Bibliography	85

Abbreviations

BTE	Boltzmann Transport Equation
BZ	Brillouin Zone
CVD	Chemical Vapor Deposition
DC	Direct Current
EPR	Electron Paramagnetic Resonance
FCC	Face Center Cubic
FEM	Finite Element Method
FWHM	Full Width at Half Maximum
GaN	Gallium Nitride
LA	Longitudinal Acoustic
LO	Longitudinal Optical
MC	Monte Carlo
NDM	Negative Differential Mobility
NDR	Negative Differential Resistivity
RF	Radio Frequency
RTA	Relaxation Time Approximation
SC	Single-Crystalline
Si	Silicon
SiC	Silicon Carbide
SRH	Shockley-Read-Hall
TCT	Transient Current Technique
TED	Transferred-Electron Device
TEO	Transferred-Electron Oscillator

TO	Transverse Optical
ToF	Time-of-Flight
UV	Ultraviolet
1D	One dimension
2D	Two dimension

1. Introduction

Scientific breakthroughs are constantly made in a vast number of areas and there is no doubt in saying that technology has made our lives easier and more convenient. Remarkable progress has for instance been made in semiconductor technology, which over the years has improved electronic devices rapidly in terms of constantly reducing their size, thus allowing the implementation of smaller and more advanced applications. These devices are changing the world we live in and are now integrated in our lives in a way that was difficult to imagine a few decades ago.

Silicon (Si) has been the dominant semiconductor material since the mid 1960's partly because it is easy to grow silicon dioxide on top of crystalline Si together with the fact that it is also an extremely common element on Earth [1, 2]. Constant improvements have been made in Si technology, but we are getting closer to actually reaching the material limits¹. Si is also not an ideal material for power electronic devices where properties such as high blocking voltage, switching frequency, efficiency and reliability are desired [3]. Another concern is that it is also not suitable for extreme applications such as being exposed to high temperatures or environments with hard radiation. While trying to overcome the drawbacks of Si, also other materials are sought for. Wide-bandgap semiconductors such as Silicon Carbide (SiC), Gallium Nitride (GaN) and diamond have superior electrical properties and are possible candidates for base materials in future power electronic devices.

SiC is the only commercially available wide-bandgap material used in power electronic devices [3]. It was already in the late 1980's anticipated that SiC could reduce energy losses and be used in practical implementations [4]. In 2015, Mitsubishi Electric Corporation had a traction inverter with all-SiC components installed on trains belonging to Odakyu Electric Railway in Japan. The company had expected energy savings between 20 - 36%² [5]. After tests had been performed over the course of four months, reports indicated an achievement of approximately 40% savings in power consumption compared to trains that used conventional circuitry³. Diamond, a semiconductor with an

¹<https://phys.org/news/2015-08-silicon-limits-power-electronics-revolution.html>, 2018-04-09

²<http://www.railwaygazette.com/news/traction-rolling-stock/single-view/view/odakyu-electric-railway-to-test-all-sic-power-module.html>, 2018-04-09

³<http://www.mitsubishielectric.com/news/2015/0622-a.html>, 2018-04-09

even larger bandgap than SiC, has the potential of reducing the losses even more [4].

Diamond has many excellent properties such as high thermal conductivity, high mobility, extremely wide bandgap, chemical inertness and high electric breakdown field. These are all important properties for a material used in power electronics and also in hazardous environments. Even though diamond has long been known as a material that has superior electronic properties when compared with Si and SiC, it is however still not so well researched. It was only in the last decade that Single-Crystalline Chemical Vapor Deposition (SC-CVD) diamond got to a state of high purity where it became more interesting to investigate its use in electronic devices [6]. Considering diamond's excellent properties together with the possibility of now growing it with high quality, there is a strong belief that it can be used in future electronic devices even in extreme environments [7, 8]. Using such high-grade SC-CVD diamond samples, our group has recently found several interesting aspects of electron behavior that occur under certain conditions [9, 10]. This thesis aims at studying the electron charge transport in SC-CVD diamond in order to get a better understanding of the conditions required for such behavior to occur. It also seeks a way of using our discovery as a foundation for the development of electronic devices.

1.1. Diamond

Diamond is a wide-bandgap semiconductor with great material properties such as extreme mechanical strength and high refractive index. It has higher carrier mobilities than Si, and with its extremely wide bandgap it also adds the benefits of high thermal stability and high electric breakdown field. Diamond is a very promising material for electronic applications since at room temperature it conducts heat ten times better than copper, which is of great benefit for power electronic devices because of its inherent ability to dissipate the generated heat associated with losses. In the growth process, it also has an advantage over other wide-bandgap semiconductors such as SiC and GaN in the sense that it has a much simpler structure consisting of only carbon atoms. It is chemically inert, optically transparent (in the visible and ultraviolet (UV) wavelengths as well as across most of the infrared wavelengths [8]) and the raw material for making diamond is cheap and comes from naturally abundant gases without any involvement of toxic substances.

1.2. Outline

This thesis begins with the theory of electron transport in diamond explained in **Chapter 2** with details about the band structure, carrier scattering mechanisms, drift velocity, drift mobility and the Boltzmann transport equation. **Chapter 3** gives an overview of the results of electron and hole drift velocities at temperatures from 10 to 470 K. Electron transport at low temperatures is also presented together with the Negative Differential Mobility (NDM) effect and the occurrence of valley-polarized electrons. **Chapter 4** explains the NDM effect in detail, which occurs within a temperature range of 100 to 150 K. This chapter also presents a way to utilize this effect in order to create a transferred-electron oscillator. An investigation into theory and the obtained experimental results is also included in this chapter. **Chapter 5** provides a background and further investigation into our group's discovery of valley-polarized electrons in diamond which is presented together with results from simulations as well as experiments. Conclusions are given in **Chapter 6**, and **Chapter 7** shortly summarizes all the included papers. Finally, **Chapter 8** presents ideas for future research.

2. Electron transport in diamond

Diamond is a wide-bandgap semiconductor with an indirect bandgap of 5.47 eV at room temperature [8]. It is a crystal containing only carbon atoms formed in a diamond lattice giving extremely strong tetrahedral bonds which provide its exceptional hardness. Being a semiconductor, it means that the conductivity is sensitive to variations in temperature, illumination and electric field. These properties are what make semiconductors special and important as base material for general electronic components. In this thesis, we are interested in the electron charge transport which is one of the important properties affecting the parameters of an electronic device.

This chapter presents diamond's band structure, phonon dispersion, carrier scattering mechanisms, carrier drift velocities and mobilities, and also the Boltzmann Transport Equation (BTE) which is very useful for deriving further equations required for this study.

2.1. Band structure

Diamond is a non-polar semiconductor since it consists of only carbon atoms. It has a Face Center Cubic (FCC) lattice in the direct (real) space with two atoms per primitive cell, where a primitive cell is a unit cell with minimum volume as seen in Figure 1 (left) [11, 12]. The reciprocal lattice in Figure 1 (right) can be obtained from the direct lattice, where its first Brillouin Zone (BZ) is a primitive cell of the reciprocal lattice in momentum- or k -space that is used to describe the conduction band.

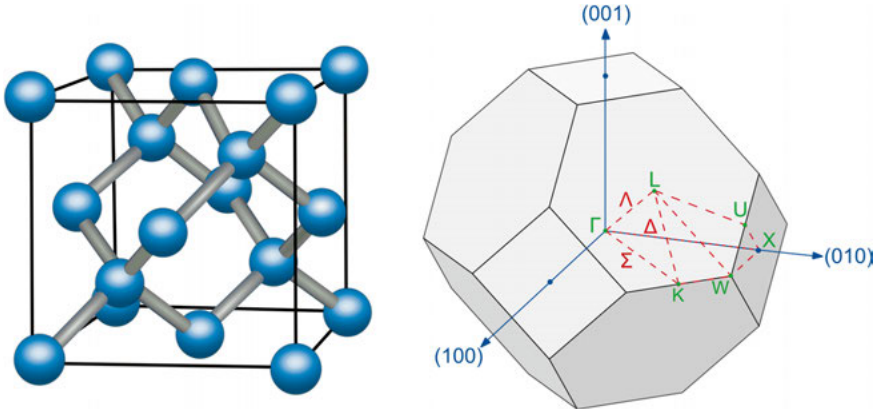


Figure 1. The diamond structure with an FCC lattice in the real space (left) and in the reciprocal space within the first BZ (right).

The energy band structure is used to explain the relationship between the energy $E(\vec{k})$ and a wavevector \vec{k} . Figure 2 (left) shows the energy band of diamond with the Gamma point (Γ) ($k = 0$) in the center of the BZ and with the X and the L points lying on the $\{100\}$ and $\{111\}$ directions, respectively. Figure 2 (right) shows the constant energy surfaces in the first BZ, where the locations of the six ellipsoids are represented by the dot in the left figure.

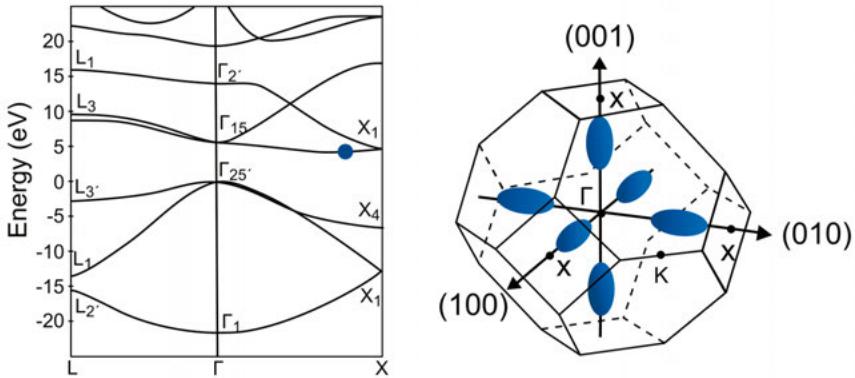


Figure 2. The energy band in diamond (left, modified from [11]) and the constant energy surfaces in the first BZ (right).

Similar to silicon, diamond has six isolated conduction band minima situated at 76% of the distance from the Γ point towards the X point in the first BZ as seen in Figure 2 [8, 13]. All have the same energy and effective mass but with a longitudinal effective mass (m_l^*) along its respective axis and a transverse effective mass (m_t^*) orthogonal to the axis. Close to the minima the electron's energy $E(\vec{k})$ can be approximated by

$$E(\vec{k}) = E_{c0} + \frac{\hbar^2}{2} \left[\frac{k_l^2}{m_l^*} + \frac{2k_t^2}{m_t^*} \right] \quad (2.1)$$

where E_{c0} is the energy at the conduction band minima (5.47 eV), \hbar is the reduced Planck constant, and k_l and k_t are the components of \vec{k} in the longitudinal and transverse direction respectively, measured from the conduction band minima.

Time-resolved cyclotron resonance measurements of optically excited carriers have yielded $m_l^* = 1.56m_0$ and $m_t^* = 0.28m_0$ [14], whereas state-of-the-art density functional theory calculations have given $m_l^* = 1.1m_0$ and $m_t^* = 0.22m_0$ (with m_0 being the electron rest mass 9.11×10^{-31} kg) [15]. Since diamond has an FCC crystal structure just as silicon does, it has a similar phonon dispersion but considerably higher phonon energies due to its rigid covalent carbon-carbon bond.

The energy dispersion gives the phonon dispersion relation between frequency and wavevector described by $E = \hbar\omega$, where ω is the phonon frequency. The phonon dispersion curve of diamond is seen in Figure 3 [16]. Phonons or lattice vibrations are a major cause of the charge carrier scattering in semiconductors. Since diamond has two atoms in a unit cell, there are six modes of oscillations with three belonging to the acoustic mode and three to the optical mode [11, 17].

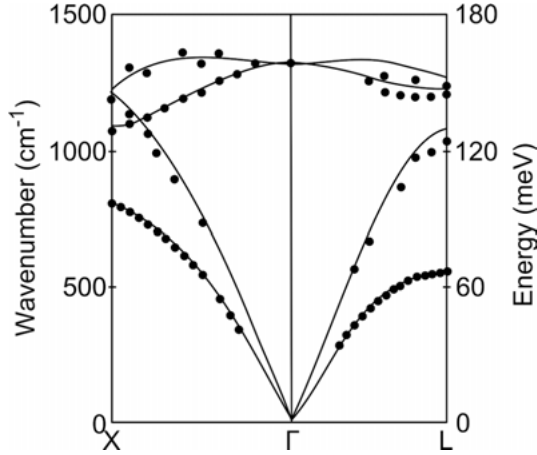


Figure 3. The phonon dispersion curve of diamond [16]. The lines indicate calculated values and the dots are gathered from experiments.

The acoustic modes correspond to sound waves which move coherently with the adjacent atoms whereas optical modes have an out-of-phase movement. The optical modes occur when the lattice base consists of more than one atom and the name arises from the fact that such vibrations interact strongly with light [18]. The curves with wavenumber zero at the Γ point are exactly three acoustic modes and the other curves are optical modes. The higher one belongs to the longitudinal mode and the lower two which lie on top of each other belong to the transverse mode and apply for both the acoustic and the optical mode. In the longitudinal mode, atoms are displaced in the parallel direction of propagation whereas in the transverse mode they are displaced in the orthogonal direction.

2.2. Scattering

Scattering of charge carriers is important to study in semiconductors for understanding the charge transport within bulk material and devices. It can occur by collision with crystal defects, such as impurities, or through interaction with phonons or other carriers. The average time between two collisions is normally referred to as the relaxation time. This determines the carrier mobility which makes it an important mechanism to study. All possible scattering mechanisms are not described here and instead we focus on the most important ones and give short explanations of them. The scattering mechanisms can be divided into intravalley and intervalley scattering, where phonon, ionized impurity and neutral impurity scattering are part of both categories. The intravalley scattering is dominated by phonons near the Γ point, where there is a clear energy difference between the optical and the acoustic branches. Intervalley scattering instead needs phonons near the zone boundary where the optical and acoustic branches have more or less the same energy and it is not so useful to distinguish between these branches anymore. The scattering mechanisms of interest are described in Figure 4.

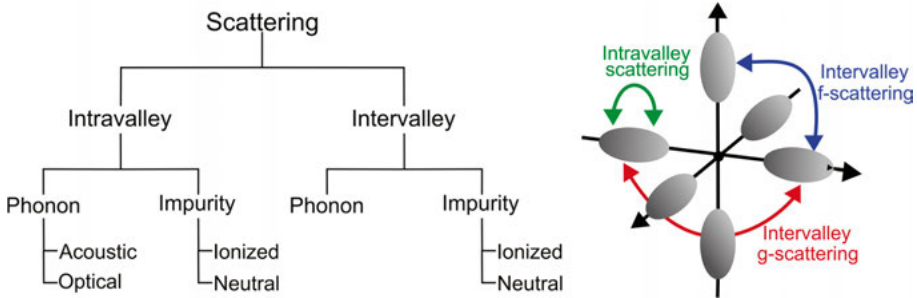


Figure 4. The hierarchy of the different scattering mechanisms of interest (left) and an illustration of intervalley and intravalley scattering (right).

2.2.1. Intravalley scattering

Intravalley scattering is a process where the initial and final state of a carrier is within the same valley, which in diamond involves both phonon and impurity scattering. Only long wavelengths are effective in intravalley scattering [18, 19].

Phonon scattering

Phonons are quasi-particles which can interact with carriers via scattering. At higher temperatures, the number of phonons increases and therefore increases the scattering rate, which in turn tends to reduce the mobility. The scattering is either optical or acoustic and can be absorptive or emissive. Longitudinal Optical (LO) phonon energies are almost three times higher in diamond (163 meV) than in silicon (63 meV) because of diamond's strong covalent bonds [8, 11, 19]. This has the implication that higher carrier energies are required in order for phonon scattering to occur in diamond and it thus has a lower phonon scattering rate than silicon.

Acoustic phonon scattering

As diamond is a non-polar semiconductor the interaction between carriers and acoustic phonons is induced by long wavelength vibrations in the lattice spacing. Acoustic phonons with long wavelengths carry little energy and thus cause nearly elastic scattering. When the acoustic deformation potential (a constant related to the energy change of an electron due to lattice deformation by acoustic phonons) is considered in a parabolic band the carrier mobility is proportional to $T_L^{-3/2}$ with T_L being the lattice temperature in Kelvin [8, 11].

Optical phonon scattering

Optical phonons with long wavelengths carry an energy ($\hbar\omega_{LO}$) of 163 meV and their scattering are considered inelastic as the high energy of the phonons causes a complete exchange of energy with the carrier [8]. Only non-polar optical phonon absorption is allowed for low energy carriers where the scattering rate is roughly proportional to the concentration of optical phonons. At temperatures below 600 K, which is well below the Debye temperature of 2240 K [20], the optical phonon concentration increases exponentially with temperature.

Ionized impurity scattering

If ionized impurities are present in a solid, holes and electrons are scattered due to long range Coulomb interaction. The rate is dependent on the concentration of the ionized impurities. For shallow impurity levels, the ionized impurity concentration (n_i) does not depend on temperature which results in a

mobility proportional to $T_L^{3/2}$. With its extremely wide bandgap, diamond has however no shallow impurity levels which makes the concentration of impurities dependent on temperature. The mobility from ionized impurity scattering is therefore proportional to $\frac{T_L^{3/2}}{n_i(T_L)}$ instead [8].

Neutral impurity scattering

The scattering cross-section for neutral impurities is normally much smaller than the one for ionized impurities. Since neutral impurities contain no net charge, their size is about the size of the cross-sectional area of the impurity atom. The mobility resulting from neutral impurity scattering is not dependent on temperature, but only on the neutral impurity density [8].

2.2.2. Intervalley scattering

Intervalley scattering is when electrons scatter between different valleys, thus involving a large change of momentum. It requires phonons with wave vectors near the zone boundary (around the conduction band minima). As diamond is an indirect bandgap semiconductor with six conduction band valleys symmetric in the BZ, intervalley scattering can occur and can be either longitudinal or transverse and in the form of optical or acoustic phonons. There are two ways for intervalley scattering to occur, named *g*- and *f*-scattering. As depicted in Figure 4 (right), *g*-scattering is the process of moving a carrier from a given valley to the one on the opposite side on the same axis whereas *f*-scattering involves moving the carrier to any of the orthogonal valleys.

Acoustic and optical phonons near the zone boundary have a lower energy than optical phonons at the Γ point. In diamond, intervalley phonon *f*-scattering requires interaction with Longitudinal Acoustic (LA) or Transverse Optical (TO) phonon modes close to the K-point at the BZ boundary. Due to the rigid covalent bonds, the K-point LA or TO phonon energies are exceptionally high in diamond, about 130 meV [21, 22].

2.3. Velocity and mobility

In general, the motion of charge carriers (electrons or holes) is random in all directions. When an electric field is applied carriers accelerate in the same or opposite direction as the field. At low electric fields and for isotropic valleys the drift velocity (\vec{v}_d) is proportional to the field (\vec{E}) with a constant scalar low-field drift mobility (μ).

$$\vec{v}_d = \mu \vec{E} \quad (2.2)$$

The electron drift mobility depends on the average relaxation time $\langle \tau_m \rangle$ and the conduction band effective mass m_c^* according to $\mu = \frac{q}{m_c^*} \langle \tau_m \rangle$, where q is the elementary charge.

Since diamond has anisotropic valleys the symmetry of the valleys will break when applying an electric field. The electrons in the two valleys in parallel to the electric field respond with m_l^* and the electrons in the four perpendicular valleys respond with m_t^* . An example is illustrated in Figure 5.

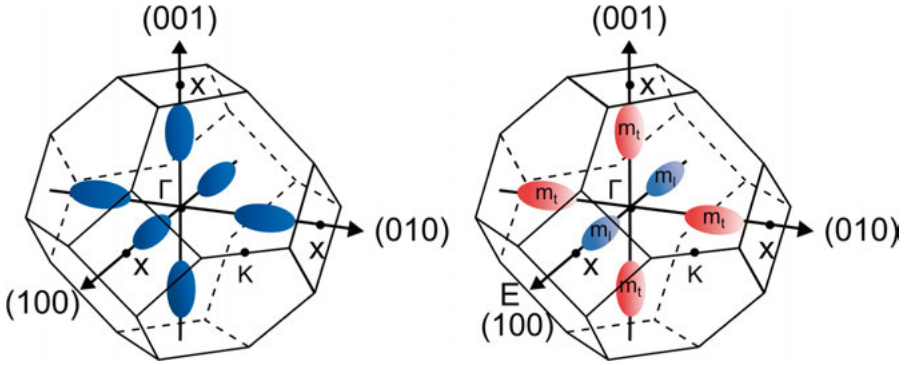


Figure 5. The six conduction band valleys in diamond along the $\{100\}$ axes with no electric field applied (left) and the effective masses seen as a response to an electric field applied in the $[100]$ direction (right). The electrons in the two valleys located on that axis (indicated blue) respond to the field with m_l^* and the electrons in the other four perpendicular valleys (axis (010) and (001), indicated red) respond with m_t^* .

The electron velocity and mobility can be considered for two distinct cases. The isotropic case has a high intervalley scattering rate thus making it impossible to distinguish between electrons with different effective mass. In the anisotropic case, there is instead a low intervalley scattering rate making it possible to observe electrons with different mobilities in certain directions.

2.3.1. Isotropic case

This is commonly observed for samples with a high impurity concentration or at high temperatures when the intervalley scattering rate is high. The drift velocity is expressed as equation (2.2). Due to the averaging effect of the rapid scattering between valleys the ellipsoidal valleys can be replaced with a single spherical valley, and the longitudinal and transverse effective masses m_l^* and m_t^* can be replaced with an equivalent conduction band effective mass m_c^* , which is given by

$$\frac{1}{m_c^*} \equiv \frac{1}{3m_l^*} + \frac{2}{3m_t^*} \quad (2.3)$$

When increasing the electric field, the average drift velocity increases until it eventually starts to saturate (v_{sat}) which causes the drift mobility to no longer be constant. In diamond, the electron saturation velocity at room temperature is around 2×10^7 cm/s [8, 23, 24] and is limited by scattering. The dependence of the drift velocity on the electric field strength can be described by an empirical relation [25–28] as

$$\vec{v}_d = \frac{\mu \vec{E}}{1 + \frac{\mu |\vec{E}|}{v_{sat}}} \quad (2.4)$$

2.3.2. Anisotropic case

This case is applicable to valley-polarized electrons with different longitudinal and transverse effective mass confined to a single valley. At low electric fields, the drift velocity is not necessarily parallel to the applied field and is given by

$$v_\alpha = \tilde{\mu}_{\alpha\beta} E_\beta \quad (2.5)$$

in Einstein notation with α, β being vector indices from the set $\{x, y, z\}$ and $\tilde{\mu}_{\alpha\beta}$ is the low-field drift mobility tensor

$$\tilde{\mu}_{\alpha\beta} = q(M^{-1})_{\alpha\beta} \langle \tau_m \rangle \quad (2.6)$$

where

$$(M^{-1})_{\alpha\beta} = \frac{1}{\hbar^2} \frac{\partial^2 E(k)}{\partial k_\alpha \partial k_\beta} \quad (2.7)$$

is the inverse of the effective mass tensor. For the electrons in the two valleys on the x -axis we have

$$(M)^{-1} = \begin{pmatrix} m_l^* & 0 & 0 \\ 0 & m_t^* & 0 \\ 0 & 0 & m_t^* \end{pmatrix}^{-1} \quad (2.8)$$

On the y -axis, we instead have

$$(M)^{-1} = \begin{pmatrix} m_t^* & 0 & 0 \\ 0 & m_l^* & 0 \\ 0 & 0 & m_t^* \end{pmatrix}^{-1} \quad (2.9)$$

and for the z -axis, the tensor is given by

$$(M)^{-1} = \begin{pmatrix} m_t^* & 0 & 0 \\ 0 & m_t^* & 0 \\ 0 & 0 & m_l^* \end{pmatrix}^{-1} \quad (2.10)$$

In the anisotropic case, the drift velocity differs depending on the direction of the applied electric field. In diamond, two different types of electrons have been observed when applying the electric field in $[100]$ direction. At a temperature of 77 K, the drift mobility was reported as $29000 \text{ cm}^2/\text{Vs}$ for the electrons in the valleys orthogonal to the electric field and $5580 \text{ cm}^2/\text{Vs}$ for the electrons in the valleys in parallel to the electric field [10].

2.4. Charge transport equations

As electrons in the two valleys along the same axis have nearly identical transport properties, no distinction between them is made in this thesis. The valleys are thus defined as illustrated in Figure 6.

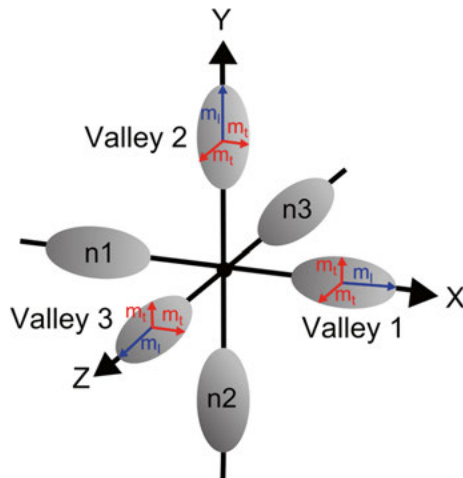


Figure 6. The two valleys on the same axis are lumped together and named $n1$, $n2$ and $n3$ for the valleys on the x -, y - and z -axis respectively.

2.4.1. Fundamental transport equations

By solving the BTE in the Relaxation Time Approximation (RTA) for the case of a Fermi gas under an applied electric field (shown in Ref. [18, 28]), the drift-diffusion equations are obtained. At location $\vec{x} = (x, y, z)$ and time t , they are given by

$$J_{p,\alpha}(\vec{x}, t) = \mu_p \left(-qp \frac{\partial}{\partial x_\alpha} \Phi - kT_L \frac{\partial}{\partial x_\alpha} p \right) \quad (2.11)$$

$$J_{ni,\alpha}(\vec{x}, t) = (\tilde{\mu}_{ni})_{\alpha\beta} \left(-qn_i \frac{\partial}{\partial x_\beta} \Phi + kT_L \frac{\partial}{\partial x_\beta} n_i \right) \quad (2.12)$$

where α and β are indices of x , y or z ; i is the valley number 1, 2 or 3; $J_p(\vec{x}, t)$ and $J_{ni}(\vec{x}, t)$ is the hole and electron current density; Φ is the electrostatic potential; k is the Boltzmann constant; $p(\vec{x}, t)$ and $n_i(\vec{x}, t)$ is the hole and electron concentration; μ_p and $(\tilde{\mu}_{ni})_{\alpha\beta}$ is the hole mobility and electron mobility tensor and T_L is the lattice temperature.

The total current density $J_{tot,\alpha}(\vec{x}, t)$ is found by the sum of Maxwell's displacement current and the current densities for electrons and holes as

$$J_{tot,\alpha}(\vec{x}, t) = J_{p,\alpha}(\vec{x}, t) + J_{n1,\alpha}(\vec{x}, t) + J_{n2,\alpha}(\vec{x}, t) + J_{n3,\alpha}(\vec{x}, t) - \epsilon_0 \epsilon_r \frac{\partial}{\partial t} \frac{\partial}{\partial x_\alpha} \Phi \quad (2.13)$$

Here ϵ_r is the relative permittivity of diamond and ϵ_0 the permittivity of vacuum. Poisson's equation gives the relationship between the free charges and the resulting electric field as

$$\frac{\partial}{\partial x_\alpha} \frac{\partial}{\partial x_\alpha} \Phi = \frac{q}{\epsilon_0 \epsilon_r} (n_1 + n_2 + n_3 - p) \quad (2.14)$$

The continuity equations are used for describing the net charge of the carrier concentration at a specific time and location when drift-diffusion occurs simultaneously with a generation rate $g(\vec{x}, t)$ and a recombination rate $r(\vec{x}, t)$. These equations are

$$\frac{\partial p}{\partial t} = g_p - r_p - \frac{1}{q} \frac{\partial J_{p,\alpha}(\vec{x}, t)}{\partial x_\alpha} \quad (2.15)$$

$$\frac{\partial n_i}{\partial t} = g_{ni} - r_{ni} + \frac{1}{q} \frac{\partial J_{ni,\alpha}(\vec{x}, t)}{\partial x_\alpha} \quad (2.16)$$

$J_{ni,\alpha}(\vec{x}, t)$ and $J_{p,\alpha}(\vec{x}, t)$ given in equation (2.11) and (2.12) used in equation (2.15) and (2.16) give

$$\frac{\partial p}{\partial t} - \mu_p \left(\frac{\partial}{\partial x_\alpha} \left(p \frac{\partial}{\partial x_\alpha} \Phi \right) + \frac{kT_L}{q} \left(\frac{\partial^2}{\partial x_\alpha^2} p \right) \right) = g_p - r_p \quad (2.17)$$

$$\begin{aligned} \frac{\partial n_i}{\partial t} + (\tilde{\mu}_{ni})_{\alpha\beta} \left[\frac{\partial}{\partial x_\alpha} \left(n_i \frac{\partial}{\partial x_\beta} \Phi \right) - \frac{kT_L}{q} \frac{\partial}{\partial x_\alpha} \frac{\partial}{\partial x_\beta} n_i \right] \\ = g_{ni} - r_{ni} \end{aligned} \quad (2.18)$$

where g_p , g_{ni} , r_p and r_{ni} are the hole and electron generation rates and the hole and electron recombination rates respectively.

2.4.2. Electron generation and recombination rate

The electron recombination rate (r_{ni}) in valley i can be found from the sum of the Shockley-Read-Hall (SRH) recombination rate ($r_{ni,SRH}$) and the electron recombination rate from the scattering out of valley i ($r_{ni,sc}$) as

$$r_{ni} = r_{ni,SRH} + r_{ni,sc} = \frac{n_i p}{n_i \tau_{n,SRH} + p \tau_{p,SRH}} + \frac{n_i}{\tau_{ni}} \quad (2.19)$$

where $\tau_{n,SRH}$ and $\tau_{p,SRH}$ is the SRH life time of electrons and holes and τ_{ni} is the scattering time out of valley i (only f -intervalley scattering is considered). The hole recombination rate is then given by

$$r_p = r_{p,SRH} = \sum_{i=1}^3 r_{ni,SRH} \quad (2.20)$$

For diamond, thermal emission across the bandgap can safely be neglected at room temperature and below. The electron generation rate is that from the scattering into valley i but in our case also optical generation is added as a laser is used to generate the electron hole pairs.

$$g_{ni} = g_{ni,optical} + g_{ni,sc} \quad (2.21)$$

The electron generation rates caused by scattering are

$$g_{n1,sc} = \frac{r_{n2,sc} + r_{n3,sc}}{2} \quad (2.22)$$

$$g_{n2,sc} = \frac{r_{n1,sc} + r_{n3,sc}}{2} \quad (2.23)$$

$$g_{n3,sc} = \frac{r_{n1,sc} + r_{n2,sc}}{2} \quad (2.24)$$

for valley $n1$, $n2$ and $n3$ respectively. The optical electron generation rate is thus in our case

$$g_{ni,optical} = \frac{1}{3} g_{p,optical} = \frac{1}{3} g_p \quad (2.25)$$

Holes will due to the applied voltage be extracted at the generation side.

3. Drift velocity in diamond

Diamond has at room temperature a thermal conductivity of 24 W/cmK [28, 29]. Intrinsic diamond can be considered as an insulator since the resistivity can exceed 10^{16} Ωcm [28, 30]. It has a very high electrical breakdown field of around 10 MV/cm [8, 28] and the low-field drift mobilities are much higher than those of Si, SiC and GaN [31]. Diamond has high carrier saturation drift velocities of 1.9×10^7 cm/s for electrons and 1.4×10^7 cm/s for holes [23]. The drift velocities have been studied in natural diamond since the 1950s [32–34] but there have also been studies performed on SC-CVD diamond [6, 23, 34].

This chapter gives an overview of results previously reported by our group [9, 10, 35–37] regarding electron and hole charge transport in SC-CVD diamond in a wide temperature range of 10 to 460 K and electric fields of 90 to 4000 V/cm. The results are presented for three temperature ranges: above 200 K, between 100 and 200 K and below 100 K (**Paper III** and **Paper V**). At temperatures below 100 K, there is a low intervalley scattering rate making it possible to distinguish between electrons with different electron polarizations. At higher temperatures, average velocities are however measured and analyzed as in the isotropic case.

3.1. At temperatures above 200 K

The results of electron and hole drift velocities at a temperature range of 200 to 460 K and electric fields of 90 to 4000 V/cm can be seen in Figure 7.

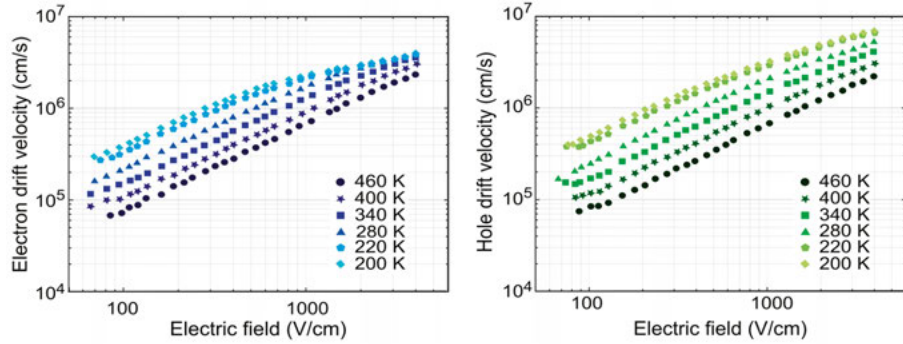


Figure 7. The electron (left) and hole (right) drift velocities at a temperature range of 200 to 460 K and electric fields of 90 to 4000 V/cm.

Within this temperature range, electrons and holes tend to exhibit a similar behavior in terms of their drift velocity as a function of the electric field. When decreasing the temperature, the drift velocities increase due to a lower scattering rate. At low electric fields, they are proportional to the electric field but at higher fields they tend to show a non-linear behavior. The drift velocities approximately obey the semi-empirical relation that was given in equation (2.4).

3.2. At temperatures between 100 and 200 K

The results of electron and hole drift velocities at temperatures between 100 and 200 K can be seen in Figure 8.

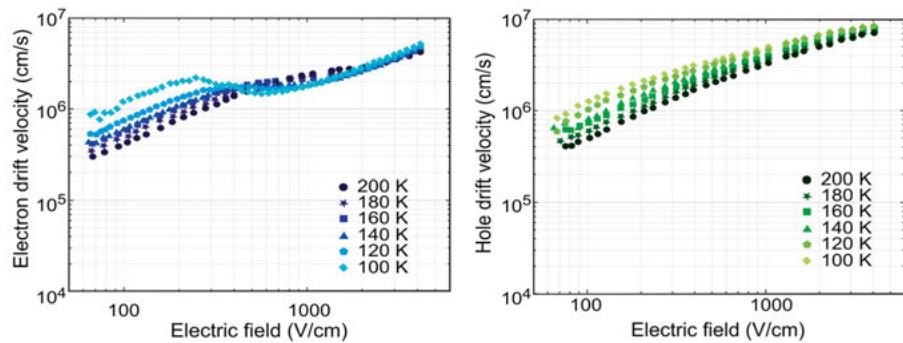


Figure 8. The electron (left) and hole (right) drift velocities at a temperature range of 100 to 200 K and electric fields of 90 to 4000 V/cm.

In the temperature interval 100 to 150 K, the behavior of electrons and holes differ and can be explained by the difference in the structure of the conduction band and the valence band. The valence band of diamond consists of three bands; the heavy-hole (*hh*), the light-hole (*lh*) and the split-off (*so*) band. The *hh* and *lh* band have their maximum energy at the Γ point of the BZ and are also degenerate there. The *so* band also has its maximum at the Γ point, but 13 meV below the *hh* and *lh* maxima [38].

The drift velocity of holes is proportional to the electric field at low fields, but saturates at higher fields. Electrons however show a non-linear drift velocity at temperatures between 100 and 150 K and electric fields between 250 and 600 V/cm [9]. This phenomenon is called *Negative Differential Mobility (NDM)* or *Negative Differential Resistivity (NDR)* and is explained in detail in Chapter 4. A comparison of the drift velocities of electrons and holes as functions of the electric field is performed at a temperature of 120 K and is seen in Figure 9.

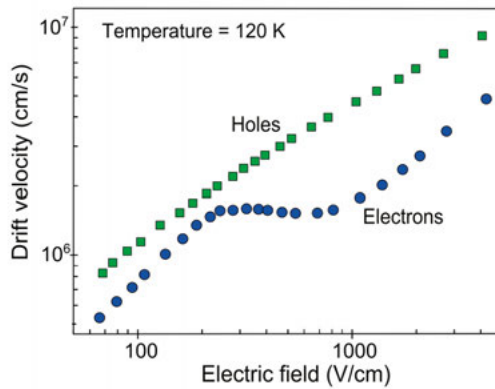


Figure 9. A comparison of the drift velocities of electrons and holes as functions of the electric field at a temperature of 120 K.

3.3. At temperatures below 100 K

The electron drift velocities at temperatures below 100 K are shown in Figure 10.

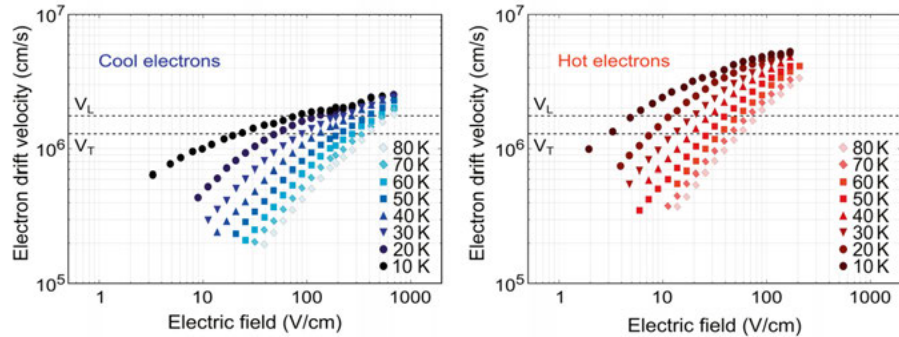


Figure 10. The electron drift velocities at temperatures below 100 K. V_L and V_T indicate the longitudinal and transverse acoustic velocities.

As was mentioned in section 2.3, that when applying an electric field in one direction the symmetry of the (otherwise equivalent) conduction band valleys will break and give rise to electrons with different effective masses, m_l^* and m_t^* . At temperatures below 100 K, the intervalley scattering rate from phonon interactions becomes low enough ($<10^4 \text{ s}^{-1}$ [37]) to make electrons more likely to stay within their valley and is the reason why two different types of electrons can be observed. The hot electrons illustrated in Figure 10 (right) represent the four valleys ((001) and (010)) orthogonal to the electric field with their mass m_t^* and the cool electrons (left) are those with mass m_l^* located in the two valleys (100) in parallel to the electric field. In diamond, the longitudinal and transverse acoustic velocities are 17.52 km/s and 12.82 km/s respectively [39]. A non-ohmic (non-linear) behavior of the drift velocity's dependence on the electric field can be observed at temperatures between 10 and 80 K due to carrier heating. A linear behavior is however seen at really low electric fields down to a temperature of 20 K [37] (**Paper III** and **Paper V**).

The hole drift velocity at temperatures below 100 K is shown in Figure 11.

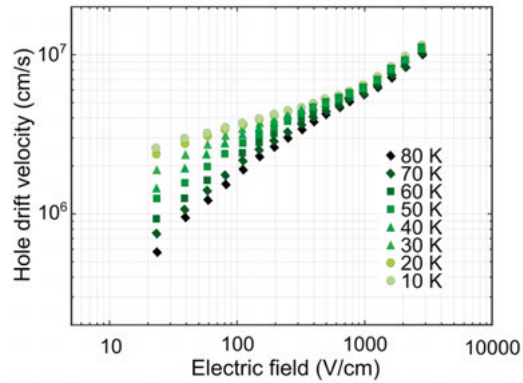


Figure 11. The hole drift velocity at temperatures between 10 and 80 K.

A slightly non-ohmic behavior is observed at very low electric fields for a temperature range of 10 to 80 K. This can be explained by the hot carrier effect [36].

4. Transferred-Electron Oscillators

The recently discovered NDM effects in diamond together with diamond's high thermal conductivity and the tremendous progress that has been made in synthesizing high quality CVD diamond makes the material a potential candidate for microwave semiconductor devices.

This chapter presents the theory behind valley repopulation which explains the NDM effect and its occurrence in diamond. It also highlights important design parameters for the fabrication of a Transferred-Electron Oscillator (TEO). Two different simulation models are presented, where the first utilizes data from experiments showing an NDM effect and the second is based on valley repopulation. The simulation results are presented together with an experimental investigation of a TEO. A summary is given at the end of the chapter.

4.1. Valley repopulation

When applying an electric field along a single direction, the symmetry of the conduction band valleys breaks and gives rise to electrons with different effective masses and velocities. When increasing the electric field, the electrons in the valleys on the axes orthogonal to the field are heated up more than the electrons in the valleys in parallel to the field due to the difference in their effective masses ($m_t^* < m_l^*$). If the electric field is high enough, the hot electrons in the orthogonal valleys reach the energy threshold for LA phonon emission (120 meV) which leads to a strong repopulation from the orthogonal to the parallel valleys [9]. With a further increase in the electric field, the electrons in the parallel valleys also reach this threshold energy and will re-scatter to the orthogonal valleys in a process called *valley repopulation*. If this repopulation rate is high enough, it is possible to observe a negative mobility for a certain electric field range. This effect is called NDM.

4.1.1. Negative Differential Mobility

Figure 12 illustrates the NDM effect and how it occurs in diamond. It is a phenomenon characterized by a local decrease of drift velocity and mobility for an increase of electric field.

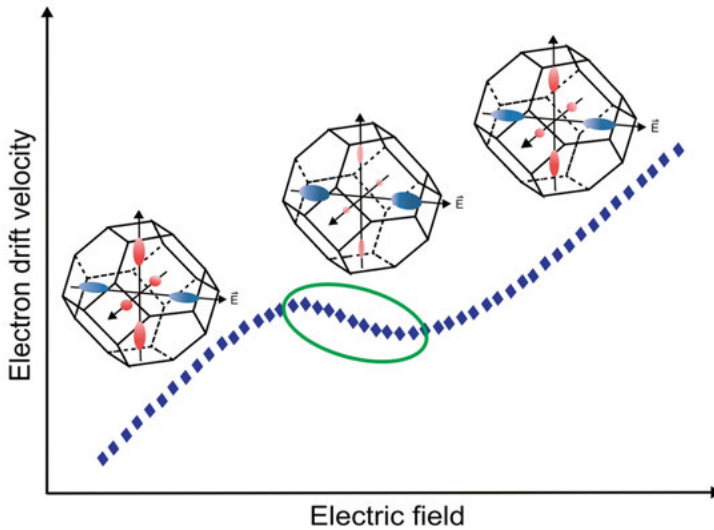


Figure 12. The electron drift velocity as a function of the applied electric field. The repopulation process makes the distribution of electrons in the orthogonal and in the parallel valleys depend on this field. The red- and blue-colored ellipses denote the hot and the cold valleys, respectively. Their size is proportional to the number of electrons occupying them.

NDM is normally observed at room temperature only in direct bandgap III-V and II-VI semiconductor materials such as GaAs, InP, InAs, ZnSe and CdTe [40–43]. As an example, GaAs has at room temperature a lower effective mass at its central conduction band valley, found at the Γ point in the BZ, than in its satellite valleys. The energy difference between these two valleys is about 0.36 eV. When the applied electric field increases, electrons with a lower effective mass at the central conduction band valley are heated and scattered into the satellite valleys where they have a higher effective mass, thus leading to an NDM effect. For GaAs, it has been observed at room temperature and electric fields above 3.5 kV/cm [40]. Our research group has, for the first time ever, observed an NDM effect in diamond even though it is an indirect bandgap group IV semiconductor where it is commonly not seen. This occurs at a temperature range of 100 to 150 K for an electric field range of 250 to 600 V/cm [9]. In order to observe the NDM effect, the diamond sample must have an impurity concentration below $\approx 10^{15} \text{ cm}^{-3}$.

4.2. Transferred electron oscillations

If NDM is pronounced enough, electric current instabilities build up and by exploiting this phenomenon a TEO for microwave applications can be constructed. Such a device can be created by applying a Direct-Current (DC) bias voltage to a Transferred-Electron Device (TED) and a resonant circuit in series. The TED or Gunn diode is one type of negative resistance oscillator which uses NDM to generate continuous electrical oscillations. It is an important device in microwave applications covering the frequency range of 1 to 150 GHz and is mainly used as a local oscillator or as a power amplifier [25, 44]. By applying an electric field within the interval giving the negative resistance, the internal space charge and electrical field distribution become unstable and oscillations occur [45]. In the TEO, the negative resistance of the TED cancels the positive resistance of the resonator and together they create a circuit without damping, thereby generating spontaneous oscillations at the resonator's frequency.

4.2.1. Simulation

Two different simulation models of a TEO was implemented. The first one is in the following called the *NDM model* and is based on a fit to the experimental results from measurements of the NDM effect using the Time-of-Flight (ToF) technique. The electrons were investigated without discriminating between different types (the isotropic case described in section 2.3.1, **Paper II**), but with a field-dependent mobility. The second model is an improved version, based on the electron repopulation between the valleys (the anisotropic case described in section 2.3.2, **Paper VII**) and is thus called the *repopulation model*.

NDM model

The first simulations performed after the discovery of an NDM effect in diamond used the NDM model, where an average value was used for the electron velocity as it is impossible to make any separation between them. It is based on our ToF measurements performed at a temperature of 110 K, where the NDM effect was most pronounced [9]. The relationship between the electric field and the electron drift velocity was found by fitting an empirical expression to the results as shown in Figure 13 (left).

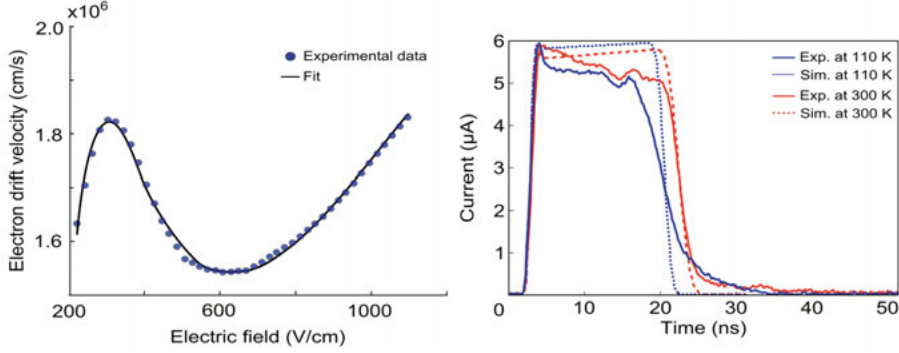


Figure 13. A fit to the electron drift velocity versus the electric field performed on data obtained from measurements on an SC-CVD diamond sample at a temperature of 110 K (left). A comparison of ToF current transients obtained from drift-diffusion simulations and ToF measurements performed at a temperature of 110 and 300 K for an applied voltage of 30 V (right).

A rational expression was suitable because it reproduces the measured data well, and from the plotted results it is obvious that at least a third order nominator was required because of the one local minima and one local maxima. The relationship between the electron drift velocity and the electric field was found to be

$$v_d = \mu_n(E)E = \frac{c_1 E^2 + c_2 E + c_3}{E^2 + c_4 E + c_5} E \quad (4.1)$$

where E is the strength of the electric field along the [100] direction. The constants were obtained from a least square's fit: $c_1 = 1.29 \times 10^3 \text{ cm}^2/\text{Vs}$, $c_2 = -349 \times 10^3 \text{ cm/s}$, $c_3 = 2.55 \times 10^8 \text{ V/s}$, $c_4 = -385 \text{ V/cm}$ and $c_5 = 6.2 \times 10^4 \text{ V}^2/\text{cm}^2$.

One (1D) and two (2D) dimensional models of a TED were simulated in COMSOL Multiphysics with its Finite Element Method (FEM) solver. The TED was based on SC-CVD diamond with a total current density given by

$$J_{tot,\alpha}(\vec{x}, t) = J_{p,\alpha}(\vec{x}, t) + J_{n,\alpha}(\vec{x}, t) - \varepsilon_0 \varepsilon_r \frac{\partial}{\partial t} \frac{\partial}{\partial x_\alpha} \Phi \quad (4.2)$$

$$J_{p,\alpha}(\vec{x}, t) = \mu_p \left(-qp \frac{\partial}{\partial x_\alpha} \Phi - kT_L \frac{\partial}{\partial x_\alpha} p \right) \quad (4.3)$$

$$J_{n,\alpha}(\vec{x}, t) = \mu_n(E) \left(-qn \frac{\partial}{\partial x_\alpha} \Phi + kT_L \frac{\partial}{\partial x_\alpha} n \right) \quad (4.4)$$

where $\mu_n(E)$ is the electric-field-dependent electron mobility seen in equation (4.1), $n(\vec{x}, t)$ is the electron concentration and $p(\vec{x}, t)$ is the hole concentration. Poisson's equation and the continuity equations are

$$\frac{\partial}{\partial x_\alpha} \frac{\partial}{\partial x_\alpha} \Phi = \frac{q}{\epsilon_0 \epsilon_r} (n - p) \quad (4.5)$$

$$\frac{\partial p}{\partial t} + \mu_p \left[-\frac{\partial}{\partial x_\alpha} \left(p \frac{\partial}{\partial x_\alpha} \Phi \right) - \frac{kT_L}{q} \left(\frac{\partial^2}{\partial x_\alpha^2} p \right) \right] = g_p - r_p \quad (4.6)$$

$$\frac{\partial n}{\partial t} + \mu_n(E) \left[\frac{\partial}{\partial x_\alpha} \left(n \frac{\partial}{\partial x_\alpha} \Phi \right) - \frac{kT_L}{q} \left(\frac{\partial^2}{\partial x_\alpha^2} n \right) \right] = g_n - r_n \quad (4.7)$$

Expression (4.1) was obtained from ToF measurements where a pulsed UV laser generated electron-hole pairs. A comparison between the simulation and the measurements was performed and is shown in Figure 13 (right), which shows a good agreement for the measured current and gives credibility to the use of drift-diffusion transport simulations. When knowing that the model was reliable, the carriers were instead generated continuously in order to achieve a continuous flux with a deep penetration depth just above bandgap. These photons get absorbed according to the Beer-Lambert law and the time-constant generation rate can be expressed as

$$g_p(x) = g_n(x) = I\kappa e^{-\kappa x} \quad (4.8)$$

where I is the photon flux, κ is the absorption coefficient and x is the penetration depth. The recombination rate is the SRH recombination rate

$$r_p = r_n = \frac{np}{n\tau_{n,SRH} + p\tau_{p,SRH}} \quad (4.9)$$

A simplified model of the TEO is illustrated in Figure 14, and the parameters used in the simulation are given in **Paper II**. A parallel RLC circuit was used to achieve a high impedance at the resonance frequency.

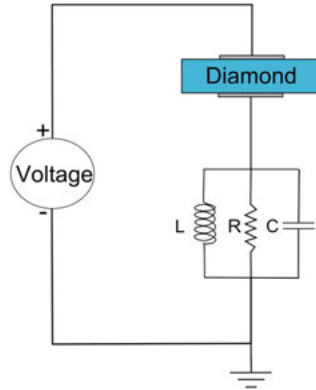


Figure 14. The simplified TEO model used in the simulation.

Free charge carriers are generated with a continuous light source and a voltage is applied over the TED in such a way that the electrons move into the bulk of the sample and the holes are attracted at the generation side. When the associated electric field in the absence of charge is within the negative resistance region, the electron concentration will grow with time. As seen in Figure 15 (left), the fast electrons catch up with the slow electrons which increases the electron density until they are extracted at the contact. This pattern is continuous and electric current instabilities build up and give rise to oscillations. This is observed as changes of current through and of voltage across the diamond over time and is illustrated in Figure 15 (middle and right).

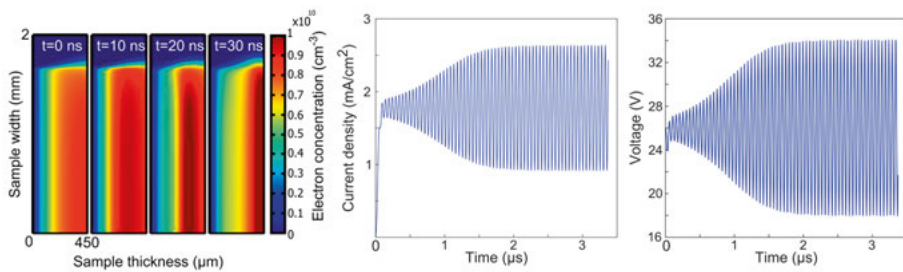


Figure 15. The electron concentration observed at different times, with the free charge carriers generated on the left side (left). The results are from the 2D simulation within half of a period at the oscillation steady-state ($> 2 \mu\text{s}$) and show that the electron cloud has grown at 10 ns and is at 30 ns extracted at the contact. It also shows the 1D simulation results of the current density through (middle) and the voltage across (right) the diamond sample as a function of time. $T = 110 \text{ K}$, $V = 26 \text{ V}$, thickness = $450 \mu\text{m}$, $L = 33 \mu\text{H}$, $C = 1.05 \text{ pF}$ and $R = 12.3 \text{ M}\Omega$. The oscillation frequency achieved with these parameters is around 20 MHz.

The 1D and 2D models agree well with each other and further investigations of varying the sample thickness and the applied voltage together with the parameters of the parallel RLC circuit were performed to achieve oscillations with a large amplitude and to reach a steady state. The results are summarized in **Paper II** and indicate that transferred-electron oscillations occur at an applied voltage of 25 to 34 V for a sample with a thickness in the range of 400 to 500 μm . The oscillation frequency varied between 10 and 20 MHz for all parameter sets. The exact values of the inductance and capacitance had no critical influence on the amplitude, but the resistance should be kept above 0.5 M Ω for oscillations to occur.

Our simulation results indicate that it should be possible to create Gunn oscillations in diamond devices at temperatures around 110 K by exploiting the occurrence of NDM. It seems that the choice of the applied voltage and sample thickness is more critical than the choice of the resonator parameters.

Repopulation model

The repopulation model takes the electron repopulation between the valleys into consideration instead of fitting an equation to the observed NDM results. It takes scattering and recombination into account while considering the anisotropic case where the electron mobility depends on the valley and the direction of the applied electric field (**Paper VII**). The mobility tensor is not considered to be dependent on the strength of the electric field, just on its direction. This is in contrast to the NDM model, where all electrons are assumed to have the same mobility and that it only depends on the electric field strength. The repopulation model is in 1D and was simulated in COMSOL Multiphysics with the aim of improving the NDM model by giving more insight into the valley repopulation effect and the results obtained.

A carrier temperature gradient term is added to the drift-diffusion equation together with the generation-recombination rate of the scattering between the different valleys. The total current density is the same as was given in equation (2.13) but the hole and electron current densities instead become

$$J_{p,\alpha}(\vec{x}, t) = \mu_p \left(-qp \frac{\partial}{\partial x_\alpha} \Phi - kT_c^p \frac{\partial}{\partial x_\alpha} p \right. \quad (4.10) \\ \left. - (\xi + 1)kp \frac{\partial}{\partial x_\alpha} T_c^p \right)$$

$$J_{ni,\alpha}(\vec{x}, t) = (\tilde{\mu}_{ni})_{\alpha\beta} \left(-qn_i \frac{\partial}{\partial x_\beta} \Phi + kT_c^{ni} \frac{\partial}{\partial x_\beta} n_i \right. \\ \left. + (\xi + 1)kn_i \frac{\partial}{\partial x_\beta} T_c^{ni} \right) \quad (4.11)$$

where $\xi = -0.85 + 0.00088(T_L - 77 \text{ K}) \text{ K}^{-1}$ is a correction factor describing the mobility's dependence on T_c^p and T_c^{ni} . In this equation, T_c^p and T_c^{ni} are the hole and electron temperatures which depend on the lattice temperature and the electric field.

The relationship between the carrier temperature and the electric field together with an evaluation of the model's reliability is described in [Appendix – Repopulation model evaluation](#). The simulations were done for a 307 μm thick diamond sample in series with a resonant circuit. The resonant circuit consisted of a 5.6 or 10 μH inductor in parallel with a 1 pF capacitor and a 10 G Ω resistor as illustrated in Figure 14. Oscillations with an amplitude between 3 and 10 V and a frequency of around 33 MHz (10 μH) and 45 MHz (5.6 μH) were observed. They occurred within a temperature range of 80 to 120 K and a voltage input range between 13 and 18 V. The current density and voltage over time at a temperature of 110 K and an input voltage of 15 V is shown in Figure 16.

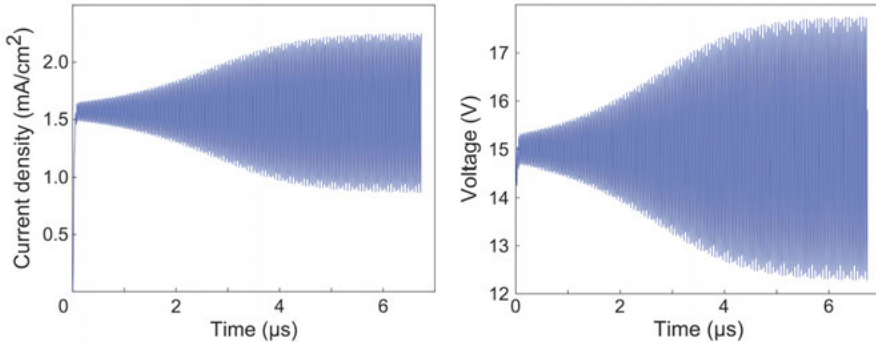


Figure 16. The current density (left) and the voltage (right) of the oscillations achieved through simulation with the repopulation model at a temperature of 110 K, an input voltage of 15 V and an inductor of 10 μH . The oscillation frequency is approximately 33 MHz.

Comparison

When comparing the NDM model and the repopulation model, it is seen that a lower current density and voltage was observed with the latter. The NDM model is based on experimental ToF measurements performed at a temperature of 110 K and suggests it to be possible to create a TEO working at that

temperature. The repopulation model indicates that it is in principle valid for a wider temperature without having to be dependent on previous NDM results. The results obtained with this model also agree with our ToF measurements, which is presented in the Appendix. The repopulation model might however not be good enough for describing the valley repopulation effects. The optimal scattering parameters and the carrier temperatures are also yet to be found. The values for acoustic deformation potential (D_A) and f -scattering deformation potential (D_f) vary among literature [46, 47] and can to some extent be explained by different input parameters or assumptions made in the models, such as the effective masses, the observed temperatures and the f -scattering threshold. Also our results have given different values, with D_A varying between 11.5 and 15 eV and D_f between 4×10^8 and 1.5×10^9 eV [9, 10, 22, 37].

4.2.2. Experiment

A theoretical investigation was performed and is presented in **Paper II** showing it is possible to create a TEO based on SC-CVD diamond. To realize this, experiments were performed with a measurement setup similar to the ToF setup used for the initial discovery of the NDM effect (**Paper VII**).

Measurement setup

The schematics of the setup is shown in Figure 17. A laser with a peak power of more than 50 mW is used, but instead of a short-pulsed UV laser of 3 ns with a wavelength of 213 nm as in our ToF setup, a HeAg laser at a wavelength of 224.3 nm and a pulse length in the 100 μ s range is used. This generates carriers continuously as the pulses are much longer than the electron transient time that happens on a 10 to 100 ns timescale. At this wavelength, the laser gives a penetration depth of 200 μ m in diamond [48]. A bias voltage is applied between the illuminated front contact and the back contact, with the negative bias at the front in order to make the electrons travel through the sample and to extract the holes at the illumination side. The contacts are deposited with Ti/Al, with the front as a semitransparent mesh on the (100) surface. This makes it possible to get a homogeneous electric field and also permits UV photons to enter the region underneath. The resulting current is amplified and measured with a fast digital oscilloscope (Tektronics TDS 684C, 5 GS/s). The sample is mounted on a gold chip sample holder and connected in series with a ferrite core inductor of 5.6 or 10 μ H and placed in a vacuum cryostat. No capacitor is added to the resonator as the capacitance of the sample is relied on instead. A shielded casing is used to isolate Radio Frequency (RF) noise generated by the outside environment and a stabilization capacitor of 33 nF is added in parallel to the bias voltage. A calibrated GaAlAs diode sensor (TG-120-CU-HT-1.4H) in conjunction with a Lake Shore 331 temperature controller is used together with liquid nitrogen as the coolant.

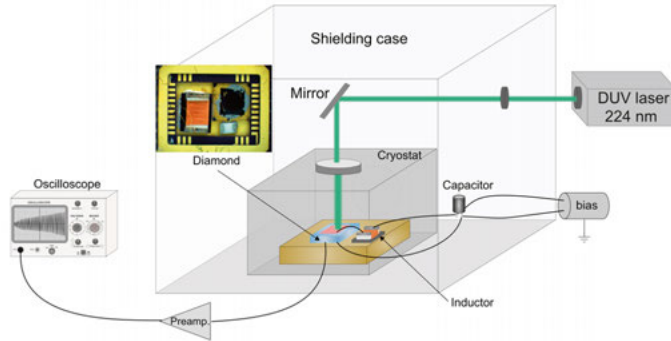


Figure 17. The measurement setup used for testing the TEO devices. The inset picture shows the sample with the resonant circuit mounted on a gold chip sample holder.

Results

The experiments were performed at a voltage range of 0 to 30 V and a temperature range of 80 to 330 K. Three SC-CVD diamond samples from Element Six Ltd. with thicknesses of 307 μm (sample A), 390 μm (sample B) and 420 μm (sample C) were used. An inductor of 5.6 μH was used for samples A and B, and 10 μH for sample C. Oscillations were observed in terms of the fundamental frequency and higher harmonics. An example of the results is seen in Figure 18 which plots the current as a function of time at a temperature of 120 K and an input voltage of 18 V.

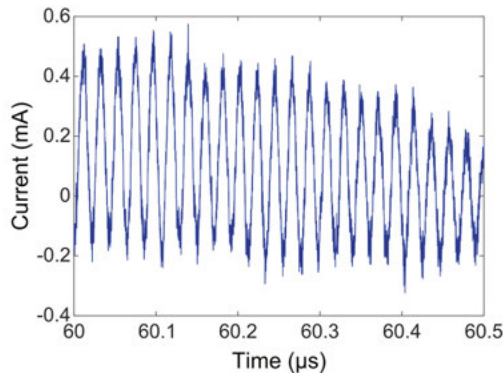


Figure 18. The current as a function of time obtained at a temperature of 120 K and an input voltage of 18 V. The measurement was performed on sample A (307 μm thick) connected in series with an inductor of 5.6 μH in parallel with a capacitor of 0.5 pF.

The Fourier transform was computed to observe the current in the frequency domain and is displayed for all three samples in Figure 19 for an input voltage of 25 V. The plots for the different temperatures are each shifted vertically in steps of 10 dB (80 K is plotted with the original values) in order to make it easier to observe the results.

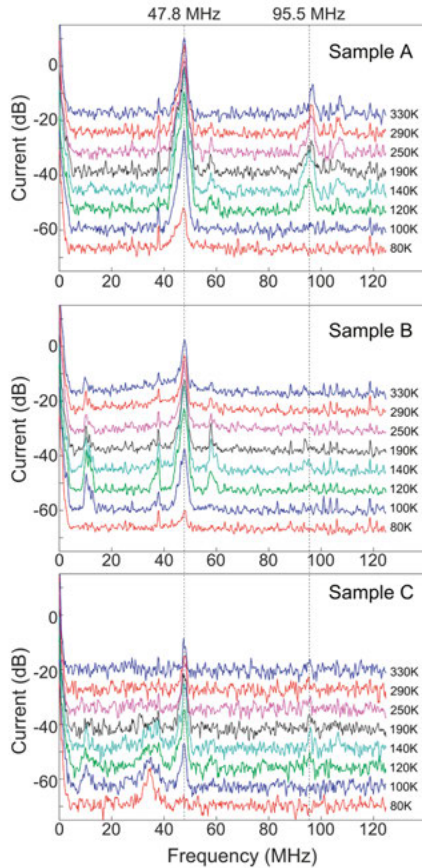


Figure 19. The current in the frequency domain for all three samples at a temperature range of 80 to 330 K and an input voltage of 25 V.

For sample A, there are two prominent peaks at 47.8 and 95.5 MHz. The first corresponds to the main oscillation clearly seen in the time domain and the higher one is its second harmonic. Sample B does not show the peak at 95.5 MHz and for sample C it is barely observable, but the oscillation amplitude in sample C is lower in general. For all samples, temperatures of around 120 to 140 K give rise to the highest peaks and thus the oscillations with the highest amplitude. At a temperature of 80 K, the 47.8 MHz peak is very small for sample A and B and not present at all for sample C. The thickness of sample B and C does not differ so much, and the use of the different sized inductor does not seem to have a big impact on the main frequency. The bigger inductor

used with sample C however gives rise to an extra peak at around 35 MHz at temperatures below 190 K.

4.3. Summary

In 2012, NDM effects were observed in diamond and explained by the repopulation of electrons in the conduction band [9]. A simulation (the NDM model, **Paper II**) of a TEO based on diamond was made based on these results and indicated that it can create oscillations. Experiments were performed and transferred-electron oscillations were observed occurring in a device based on diamond. Surprisingly, it seems that oscillations also occur outside the range of where NDM has been observed, and more analysis is needed in order to explain this. It is believed that the oscillations found are not related to any external noise as precautions were made to avoid this. In order to explain the experimental results and to improve the understanding of the NDM phenomenon in diamond, the repopulation model was created. The results obtained agreed with our ToF measurements, but might not be good enough for describing the valley repopulation effects. The discrepancy of the obtained values for D_A and D_f can be one of the reasons and needs to be analyzed further in order to improve the model.

5. Valleytronics

Valleytronics is a newly defined term and is similar to spintronics, but instead of using the electron spin the polarization of the electrons in the conduction band valleys is used to encode information. Digital electronic circuits use the presence or absence of charge to encode information which relies on a rapid redistribution of mobile charge carriers. This requires energy and results in losses which thus set a maximum limit to the switching frequency of semiconductor devices. This issue can be mitigated by using alternative methods such as spintronics [49] or valleytronics [10].

A few years ago, our group observed valley-polarized electrons in high purity diamond at temperatures below 100 K [10]. The first part of this chapter is dedicated to describing this observation. This is followed by a further investigation into the stability of the polarized electrons and their behavior within a temperature range of 10 to 80 K (**Paper III** and **Paper IV**). A study of magnetotransport is then presented, which describes how valley-polarized electrons react in the presence of a magnetic field perpendicular to an electric field (**Paper I**). This work has led to simulations and experiments of creating valley-transistors, which is also presented (**Paper VI**). Finally, the results are summarized.

5.1. Valley-polarized electrons

Diamond has six equivalent conduction band valleys oriented along the $\{100\}$ axes with a uniquely low scattering rate between them. Short wavelength lattice vibrations are required for intervalley scattering, but are at low temperatures non-existent in diamond due to the rigid lattice. Intervalley phonon scattering then becomes negligible making electrons stay in their valley which in turn leads to a stable valley polarization state. It is then possible to observe non-equilibrium valley populations (valley-polarized electron ensembles). Valley-polarized states have been observed in several materials such as MoS_2 , silicon, AlAs quantum wells, bismuth, graphene and diamond [10, 50–58].

As mentioned in section 2.3, two distinct types of electrons from different valleys can be observed in diamond when applying an electric field. An example of experimental data is illustrated in Figure 20.

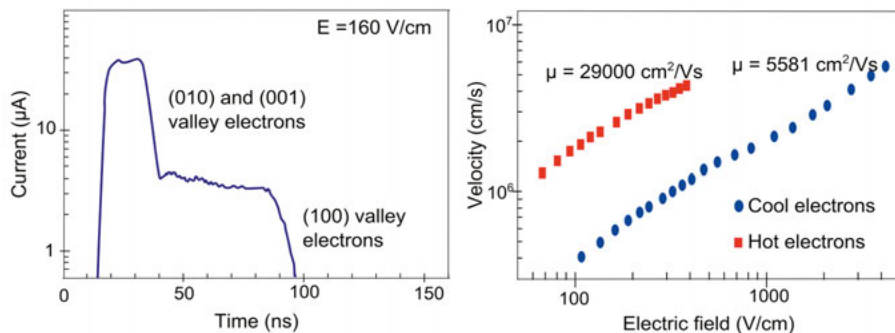


Figure 20. A current trace observed when applying an electric field of 160 V/cm along the [100] direction (left). Electrons from the valleys on the (010) and (001) axes are faster than the electrons from the valleys on the (100) axis. The velocity of hot and cool electrons as a function of the electric field for a temperature of 70 K (right).

The hot electrons in the valleys orthogonal to the electric field have a higher drift velocity than the cool electrons in the valleys in parallel to the electric field. This phenomenon of several discrete states makes new interesting electronic devices possible. Experiments performed at a temperature of 77 K show that the electrons have a relaxation time of around 300 ns and can at low electric fields be transported across a distance of 0.7 mm with only a negligible polarization loss [10]. This indicates a possibility to use the valley polarization to encode, transport and decode information and could be a viable route towards quantum computing applications.

5.2. Polarization stability

In order to make useful devices, the valley-polarized electrons must retain their polarization for a long enough time in order to allow manipulations to be performed on them. As an example, the valley polarization occurring in monolayer MoS₂ was retained for only 1 ns [50].

The stability of the valley polarized states was investigated by considering the electron-phonon deformation potential coupling in Monte Carlo (MC) simulations, where the deformation potential constants were determined from ToF measurements. Through the strength of this coupling, the relaxation time was determined from simulations as a function of temperature and the applied electric field (**Paper IV**).

5.2.1. Experiment

ToF (also called Transient Current Technique, TCT) is a powerful method for studying the electrical properties of semiconductors with high resistivity and low carrier concentrations. This technique is superior to Hall Effect measurements for samples with high resistivity and wide bandgap, such as intrinsic diamond. It can be used to study the charge transport in diamond by measuring the drift velocities and therefore the mobilities of electrons and holes, but also to observe valley-polarized electrons. With this technique, electron-hole pairs can be created by several methods, but in our case (Figure 21) performed using a short-pulsed UV laser. After creation, the free charge carriers drift in an applied electric field and the induced current at one of the contacts is measured.

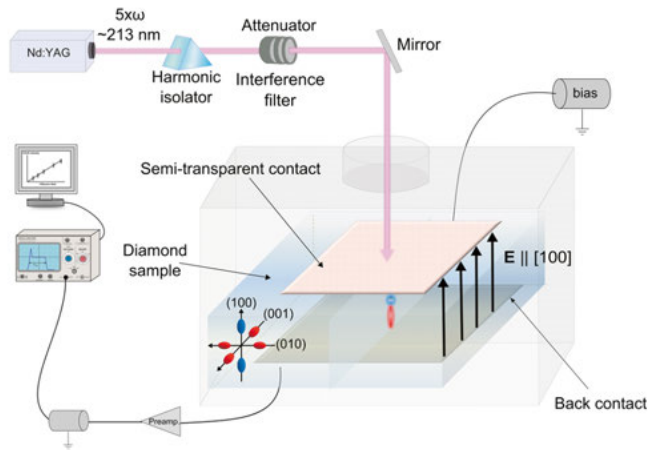


Figure 21. The ToF measurement setup.

A short UV pulse of 3 ns Full Width at Half Maximum (FWHM) is used to generate free charge carriers. Care is taken that only a little free charge (Q) is created in order not to disturb the applied electric field, which is the case if $Q \ll CU$, where C is the sample capacitance and U the applied voltage. The quintupled Nd:YAG laser has a 10 Hz repetition frequency and 213 nm wavelength, which corresponds to a photon energy just above the diamond bandgap of 5.47 eV. Several interference filters are used for blocking lower harmonics and additional neutral density filters allow for reducing the intensity to the desired magnitude. A bias voltage is applied between the top and the back contact. Semitransparent Ti/Al mesh contacts are deposited on two opposite (100) faces of the sample, which makes it possible to obtain a relatively homogenous electric field and allows for UV photons to enter the region underneath. Due to the strong light absorption of 213 nm in diamond, electron-hole pairs are only created within the first few micrometers. By choosing a certain polarity of the applied bias, the type of carrier that drifts through the bulk of

the sample towards the back contact can be controlled. In the case of valley polarization, the electron transport is investigated by applying a negative bias to the top contact. The holes are then directly collected at the top contact and the electrons are swept through the sample towards the back contact. To detect the induced current, a low-noise broadband current amplifier with a bandwidth of 1 GHz and a gain of 24 dB is used together with a digital storage oscilloscope. The bias across the sample is applied using a pulser via a bias-tee. A pulsed voltage with a 50 μs duration synchronized with the UV pulses is used to minimize the charge accumulation that might otherwise occur in the sample. The sample is mounted in a ceramic chip carrier, wire bonded and placed in a liquid nitrogen- or helium-cooled Janis ST-300MS vacuum cryostat with UV optical access. The temperature is monitored using a LakeShore 331 temperature controller with a calibrated TG-120-CU-HT-1.4H GaAlAs diode sensor in good thermal contact with the sample.

For these experiments, two single-crystalline high-purity samples with a thickness of 490 and 510 μm synthesized by Element Six Ltd. were used. The induced current was measured within a temperature range of 10 to 80 K for electric fields of 100 to 1000 V/cm. The transient times were obtained with ToF measurements by the difference between the rising and the falling edges of the induced current pulses.

5.2.2. Simulation

The simulation model was built with a simplified conduction band structure consisting of six parabolic anisotropic (ellipsoidal) valleys. This simplification is adequate at the moderate electric fields considered, and is beneficial as it reduces the computational effort considerably compared to full-band simulations. Acoustic phonon intravalley scattering was treated through inelastic deformation-potential interaction (D_A) and intervalley f -scattering as deformation-potential interaction (D_f). The probability for direct g -scattering to occur is substantially lower than for f -scattering due to a higher barrier of 165 meV. It is therefore more likely that repopulation between valleys on the same axis occurs via two subsequent f -scattering events than through one single g -scattering event, making g -scattering irrelevant in our study. Only D_A and D_f were used as free parameters in the simulation and fitting them to the ToF data gave $D_A = 12.0 \pm 1.0$ eV and $D_f = (4.0 \pm 1.5) \times 10^8$ eV/cm.

5.2.3. Results

Calculations of the induced current were performed on the simulation model and compared with the experimental results. Three different features were observed and were presented in **Paper IV**. The polarization stability of the electrons was with the simulation found by fitting their transient times when moving across the sample. The relaxation times were calculated from the electron-phonon deformation potentials and are in Figure 22 (left) seen for an electric field of 0 and 100 V/cm with varying temperatures. The relaxation times as functions of the applied electric field at a temperature of 77 K can be seen in Figure 22 (right).

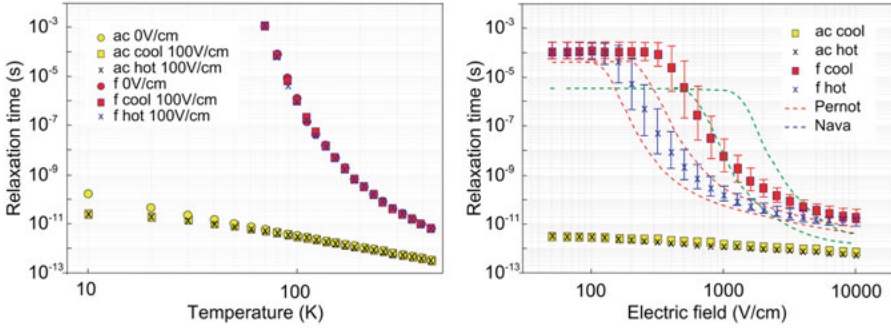


Figure 22. MC simulation results of the relaxation times of electrons in hot and cool valleys at 0 and 100 V/cm for acoustic intravalley scattering and f -intervalley scattering (left). The relaxation times for electrons initially resident in hot and cool valleys at a temperature of 77 K and electric fields below 10 kV/cm for acoustic intravalley scattering and f -intervalley scattering (right). Error bars indicate the minimum and maximum values when D_A and D_f are varied within given error limits. Corresponding curves for f -intervalley scattering using input values taken from Nava et al. [46] and Pernot et al. [47] are also plotted for comparison.

The stability of the valley-polarized states was independent of the electric field up to 100 V/cm and the relaxation time was in the microsecond time-scale at temperatures below 100 K. At higher electric fields, rapid heating of the electrons followed by phonon emission in an f -scattering event dramatically reduced the relaxation time. At fields as high as 600 V/cm it had reduced substantially for the hot valleys. The relaxation time for acoustic deformation potential intravalley scattering is much shorter due to the lack of a barrier. The electron mobility is then dominated by intravalley phonon scattering, while g -scattering is irrelevant and only f -scattering causes de-polarization.

Neutral and ionized impurity scattering and electron-electron scattering can also cause de-polarization but they were not included in the simulation model. Retaining a long polarization time therefore requires samples with low impurity concentration and low concentrations of free carriers. The influence of

ionized impurity scattering was thus minimized by selecting the purest CVD diamond samples available with a concentration of nitrogen impurities below 10^{13} cm^{-3} . A negligible carrier-carrier scattering rate was assured by controlling the amount of carrier generation and thereby limiting the free electron density to below 10^{10} cm^{-3} . The band-to-band recombination time was not considered, but it can exceed several microseconds in indirect bandgap materials.

The stability of the polarized states has been found to strongly depend on temperature and electric field strength due to the electron-phonon interaction. The relaxation time varies over several orders of magnitude when the temperature and the electric field are changed. At temperatures below 100 K and electric fields below 100 V/cm the relaxation time can be very long, even microseconds, and it is possible to use the polarization state for encoding, transporting and decoding information. In order to use diamond in valleytronic applications, one would however be restricted to low enough temperatures. Even though ionized impurities and electron-electron scattering were not considered in the simulations, they may still cause de-polarization and thus high purity and low carrier concentrations are therefore important factors.

5.3. Conduction band transport

To improve the understanding of the mechanisms involved in the conduction band transport of valley-polarized electrons, their drift velocities were measured at a temperature range of 10 to 80 K for very low electric fields, well below 10 V/cm (**Paper III**). The results were compared with MC simulations to identify the dominant scattering mechanisms. The effects of carrier heating and inelastic phonon-electron scattering were also investigated and the momentum relaxation rate for electrons with different valley polarizations as a function of temperature was found.

5.3.1. Experiment

A ToF technique was used to perform measurements on two SC high-purity samples with a size of $4.5 \times 4.5 \text{ mm}$ and thicknesses of 510 and 690 μm synthesized by Element Six Ltd. In difference to the ToF setup presented in section 5.2.1, a passively Q-switched UV laser with FWHM pulses of 800 ps and a wavelength of 213 nm at a repetition rate of 300 Hz was used instead. The light was focused onto the sample surface at a circular spot with a diameter of 2 mm. Ti/Al (20/300 nm) semitransparent mesh contacts with a diameter of 3 mm were deposited on the two opposite (100) faces and the samples were mounted on a ceramic chip carrier and placed in a liquid-helium cooled vacuum cryostat in order to achieve temperatures below 80 K.

5.3.2. Simulation

MC simulations were performed in the same way as was presented in section 5.2.2 where a simple conduction band structure was used. Acoustic phonon scattering was treated through inelastic deformation-potential interaction, but optical phonon scattering was neglected at these temperatures and electric fields. The impact of impurity scattering in the ultra-pure samples (impurity concentration $< 10^{14} \text{ cm}^{-3}$ [35] and ionized impurity concentration $< 10^{12} \text{ cm}^{-3}$ [36]) was considered to be quite small. The effect of anisotropy (the transverse and longitudinal phonon mode) is not large [59] so only one deformation potential tensor was considered. The acoustic deformation potential D_A was assumed to be 11.5 eV as it gave the best fit to the ToF results and is still within the limits of our previous study (section 5.2). The longitudinal and transverse effective masses were considered to be $1.56m_0$ and $0.28m_0$.

5.3.3. Results

The drift velocities for a temperature range of 10 to 80 K and electric fields below 700 V/cm are shown in Figure 23 together with the results from the simulations.

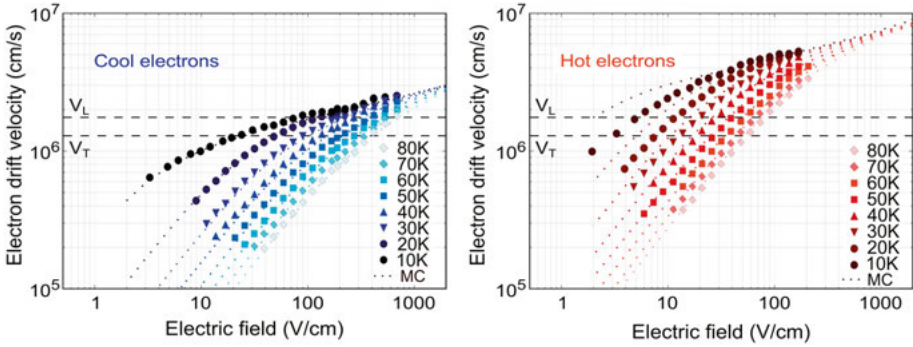


Figure 23. A comparison between the electron drift velocities of cool (left) and hot (right) electrons obtained with MC simulations and experiments performed at a temperature range of 10 to 80 K. The dotted lines are traces from the simulation and the dashed horizontal lines indicate the longitudinal and transverse sound velocity in diamond.

The results show a strong non-ohmic behavior at low lattice temperatures and high electric fields. This is explained by carrier heating which makes the carrier temperature (T_c) become substantially larger than T_L . In contrast, for electric fields below around 100 V/cm at a temperature of 80 K or electric fields below around 20 V/cm at a temperature of 20 K, carrier heating is negligible and ohmic behavior is observed. The deviation for hot valley electrons

between the experimental data and the simulation at the lowest temperatures indicates some influence of impurity scattering.

The electron mobilities were extracted for very low electric fields and seem to be linearly dependent on the lattice temperature down to 20 K. In Figure 24, the low-field electron drift mobilities are plotted as functions of lattice temperature and compared with inelastic theory for deformation potential scattering as well as with elastic approximation where the mobility is dependent on temperature ($\mu \propto T^{-3/2}$).

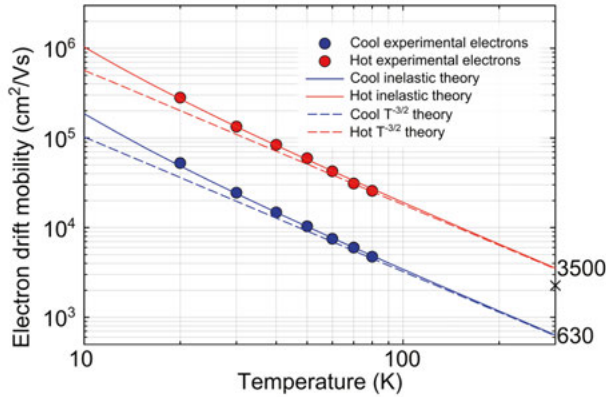


Figure 24. The low-field electron drift mobilities as functions of temperature compared with inelastic theory for deformation potential scattering (solid lines) as well as with the $T^{-3/2}$ behavior obtained from the elastic approximation (dashed lines). The cross indicates the measured effective electron mobility ($2200 \text{ cm}^2/\text{Vs}$) at 300 K.

From these results it can be observed that the measured mobilities were slightly higher than the $T^{-3/2}$ law indicates. The results however agree really well with the inelastic theory for deformation potential scattering, which takes the exchange of energy between the phonon and the electron into account. This can be attributed to the breakdown of the elastic approximation at low temperatures [60]. When absorbing (emitting) a phonon, the electron gains (loses) energy, which in turn leads to an increase (decrease) in the number of available electron states to scatter into. This becomes more pronounced at low carrier energies and therefore at low temperatures. The elastic approximation agrees well with measurements at 80 to 300 K. At temperatures higher than that, the mobilities decreased more rapidly than the $T^{-3/2}$ law indicates due to the onset of optical phonon scattering.

By extrapolating the electron mobilities measured below 80 K, we found $\mu_{hot} = 3500 \text{ cm}^2/\text{Vs}$ and $\mu_{cool} = 630 \text{ cm}^2/\text{Vs}$ at a temperature of 300 K. This combines to an effective mobility for equi-populated valleys as $\mu_{eff} = \frac{2}{3}\mu_{hot} + \frac{1}{3}\mu_{cool} = 2540 \text{ cm}^2/\text{Vs}$. The measured effective mobilities at 300 K was $2200 \text{ cm}^2/\text{Vs}$, which is slightly lower. This difference can however be

explained by the start of optical phonon scattering occurring at room temperature, giving a small reduction in mobility. The measured mobilities gave a good agreement with previously observed values [35, 61] and by adapting the simulation in order to achieve the same mobilities the relaxation rate was found. The momentum relaxation rate (inverse relaxation time) of the hot and the cool electrons as a function of temperature is plotted in Figure 25.

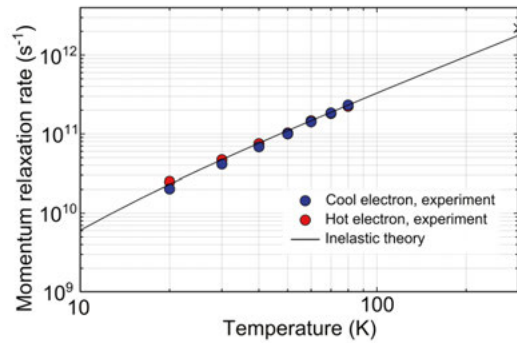


Figure 25. The momentum relaxation rate obtained by comparing drift mobility data with MC simulations. The cross indicates the momentum relaxation rate computed from mobility measurements performed at a temperature of 300 K.

Non-ohmic behavior in the temperature interval 10 to 80 K was observed and explained by carrier heating. The electron mobilities for hot and cool valleys were extracted at very low electric fields. At the lowest measured temperatures, the mobilities were substantially higher than the simple $T^{-3/2}$ law indicates and was considered as due to the breakdown of the elastic approximation of electron-acoustic phonon scattering. The effects of inelastic scattering have not in any semiconductor previously been directly observed for free carriers in a drift velocity measurement. By comparing mobility data to simulations, it was also possible to obtain the momentum relaxation rate of the valley-polarized electrons.

5.4. Magnetotransport

By using ToF, it is possible to observe electrons in one of two different states, either in the valleys orthogonal or in parallel to the electric field. A previously developed method called *Magneto-ToF* (**Paper I**) works by applying a magnetic field perpendicular to the electric field in analogy with Hall Effect experiments. This gives rise to additional non-isotropic contributions to the mobility tensor which makes it possible to observe the influence of the magnetic field on carrier transport using time-resolved current measurements. This allows studying the charge transport properties, magnetotransport and the dom-

inant scattering mechanisms in high resistivity materials. It also makes it possible to distinguish electrons with three different polarizations (without making any distinction between the electrons in the two valleys on the same axis).

5.4.1. Experiment

The Magneto-ToF setup is illustrated in Figure 26 and is similar to the ToF method mentioned in section 5.2.1 with the addition of an electromagnet applying a magnetic field between -1 and 1 T perpendicular to the electric field. Measurements were performed on three SC-CVD diamond samples with thicknesses of 490 , 510 and 690 μm . They were produced and supplied by Element Six Ltd and are in the following referred to as sample A, B, and C respectively. The nitrogen impurity level for each sample was below $5 \times 10^{14} \text{ cm}^{-3}$ determined by Electron Paramagnetic Resonance (EPR) measurements. The samples were metallized with Ti/Al by physical vapor deposition on opposite (100) surfaces and patterned by standard lithography processes. The circular front contact was made as a semitransparent mesh 4 mm in diameter.

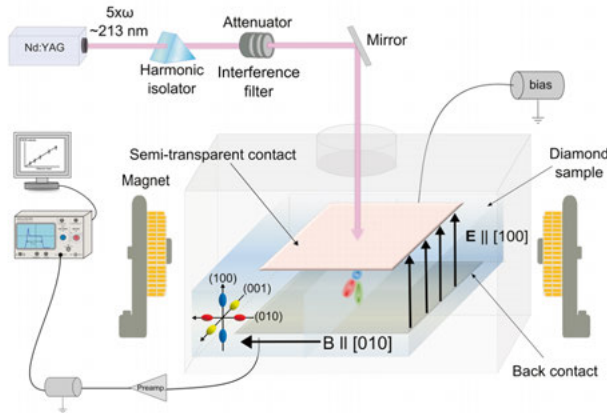


Figure 26. The setup of Magneto-ToF, which compared to conventional ToF includes an electromagnet that applies a magnetic field of up to 1 T perpendicular to the electric field.

5.4.2. Simulation

The observed magnetotransport of the valley-polarized electrons were compared both with MC simulations and an analytical model based on the BTE. The changes in the magnetic (B) field dependent mobility tensor $\tilde{\mu}_{\alpha\beta}(\vec{B})$ are relatively small and therefore a strong magnetic field ($\mu B \gg 1$) was required. The expression for $\tilde{\mu}_{\alpha\beta}(\vec{B})$ can be derived from the BTE in the RTA. By assuming power law scattering we find [18, 62–64]:

$$\frac{\tilde{\mu}_{xx}}{\mu_{xx}} = \Gamma\left(\lambda + \frac{5}{2}\right)^{-1} \int_0^\infty \frac{s^{\lambda+3/2} e^{-s}}{1 + \frac{9\pi}{16} \mu_{xx} \mu_{zz} B_y^2 \Gamma\left(\lambda + \frac{5}{2}\right)^{-2} s^{2\lambda}} ds \quad (5.1)$$

where $s = E/kT$, E is the energy, μ_{xx} , μ_{yy} and μ_{zz} are components of the zero B -field mobility tensor where the magnetic field is in y -direction (parallel to $[010]$ as indicated in Figure 26) and $\Gamma()$ denotes the gamma function. Acoustic phonon scattering (*ac*), neutral impurity scattering (*ni*) and ionized impurity scattering (*ii*) were all assumed to be in the form of power law scattering according to $\tau = c_\lambda E^\lambda$, where $\lambda = -\frac{1}{2}, 0, \frac{3}{2}$.

5.4.3. Results

The experimental effective mobilities as functions of the magnetic field at a temperature of 70 K are plotted in Figure 27. For comparison, expression (5.1) is also plotted using the experimental $B = 0$ for the mobilities μ_{xx} , μ_{yy} and μ_{zz} . The results from the MC simulation for the case of acoustic phonon scattering are also included. More details can be found in **Paper I**.

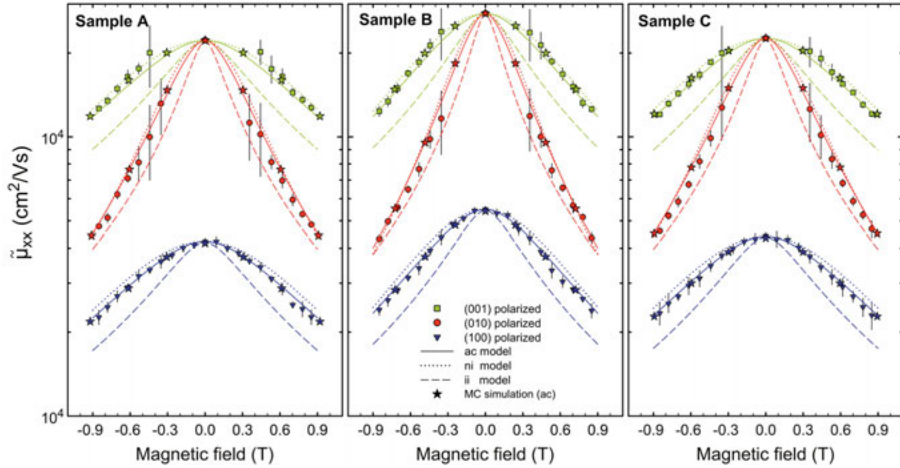


Figure 27. The measured effective mobilities at a temperature of 70 K for electrons with different valley polarizations when the electric field is applied along $[100]$ and magnetic field along $[010]$. It also includes fits for acoustic phonon deformation potential scattering (*ac*), neutral impurity scattering (*ni*) and Conwell-Weisskopf ionized impurity scattering (*ii*). Only the acoustic phonon scattering model is in agreement with the observed data in this case. The results from the MC simulation are also plotted as a comparison.

Comparing the model of the BTE to the experimental results of the magnetic-field-dependent mobilities, it can be seen that for $\lambda = -1/2$ (*ac* scattering) the curve fits the data well, while for $\lambda = 0$ (*ni* scattering) and $\lambda = 3/2$ (*ii* scattering) the agreement is poor. This permitted us to conclude that acoustic phonon scattering was the dominant electron scattering mechanism in these samples at the temperature 70 K. This conclusion holds for each of the three valley polarizations separately where we do not distinguish between valleys on the same axis. The measured longitudinal and transverse mobilities (μ_l and μ_t) at the temperature 70 K and at zero magnetic field were 4230 cm²/Vs and 22200 cm²/Vs for sample A, 5490 cm²/Vs and 27700 cm²/Vs for sample B, and 4450 cm²/Vs and 22700 cm²/Vs for sample C. Therefore, samples A and C exhibit $\sim 20\%$ lower zero *B*-field mobilities than sample B. If an intrinsic mechanism such as phonon scattering would be the only mechanism that determines the electron mobility, we would have expected to find the same mobility for all samples. Thus, a residual influence of some extrinsic mechanism is required to explain the difference. Neutral impurity scattering is a possible candidate. The difference in magnetic-field dependence between *ni* and *ac* scattering was not large and an additional contribution from *ni* scattering of 20% was not possible to resolve in our data. On the other hand, a 20% additional contribution from ionized impurity scattering was excluded. Another possible cause could be variations in the density of dislocations, which may also contribute to scattering and introduce inhomogeneities in the electric field distribution.

5.5. Valley-transistor

Valley-polarized electrons have been proposed to be exploited for usage in quantum computing [10, 22]. After the discovery of valley polarization in diamond together with the investigation presented in section 5.2, an attempt of creating a valley-transistor was performed (**Paper VI**). Based on our previous studies we know that it is possible to distinguish between two or even three different type of electrons through the use of an electric field or a magnetic field perpendicular to an electric field [10, 22, 65]. We also know that at temperatures below 100 K and electric fields below 100 V/cm, the relaxation time of electrons can be very long (microseconds) and valley-polarized electrons can therefore be transported across macroscopic distances. These findings indicate that it is possible to use the electron valley polarization for encoding, transporting and decoding information.

A transistor was the device of our choice because it allows for applying an electric field in different directions to control the electron transport within the sample. Firstly, only two different types of electrons were considered by ap-

plying only an electric field, and not a magnetic. Since this was the first attempt ever of creating a valley-transistor based on diamond, both theoretical computations and experiments were explored.

5.5.1. Simulation

A 2D model of a double-gate diamond transistor was simulated in COMSOL Multiphysics based on the drift-diffusion equations that were discussed in section 2.4.1. The geometry of the device used in the simulation is shown in Figure 28.

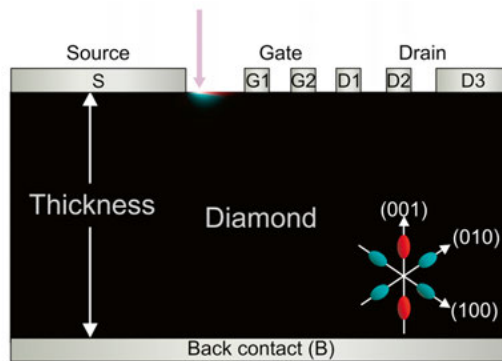


Figure 28. The geometry of the device used in the simulation with the purple arrow indicating the generation area.

The transistor was created with a geometry matching those of the samples used in the experiment and included one source contact (S), two gate contacts (G1 and G2) and three drain contacts (D1, D2 and D3) on the top and one back contact (B) on the bottom. All contacts were deposited on (001) surfaces and the top contacts were added in parallel on [110] direction in order to observe only two different type of electrons. There was no difference between the electrons on (100) and (010), except that they drift differently into and out from the plane. If the source, gate and drain contacts instead were deposited in parallel to direction [010] or [100], the electrons in the different valleys would respond differently thus allowing three distinct types to be observed.

The charge transport was for the holes and the differently valley-polarized electrons simulated using macroscopic transport equations. A laser with a short pulse duration and a wavelength of 213 nm was used to generate carriers close to the source contact. The generation rate is expressed by equation (4.8) and an absorption coefficient of $3.33 \times 10^3 \text{ cm}^{-1}$ was used.

Results

When generating electron-hole pairs close to the sample surface and the source contact, the polarity of the voltage and direction of the electric field

cause holes to be extracted at the source contact and electrons to move into the sample below the gates towards the drain contacts. In our simulation, we could separately apply different voltages between all contacts. Figure 29 shows, at different time instances, the electron transport in a sample with a thickness of $490 \mu\text{m}$ for the case of a source voltage $V_S = -7 \text{ V}$, gate voltages $V_{G1} = -5 \text{ V}$, $V_{G2} = -2.4 \text{ V}$ and back voltage $V_B = -2.4 \text{ V}$. All voltages are referenced to the drain contacts, which are connected to ground. The lines correspond to the equipotential.

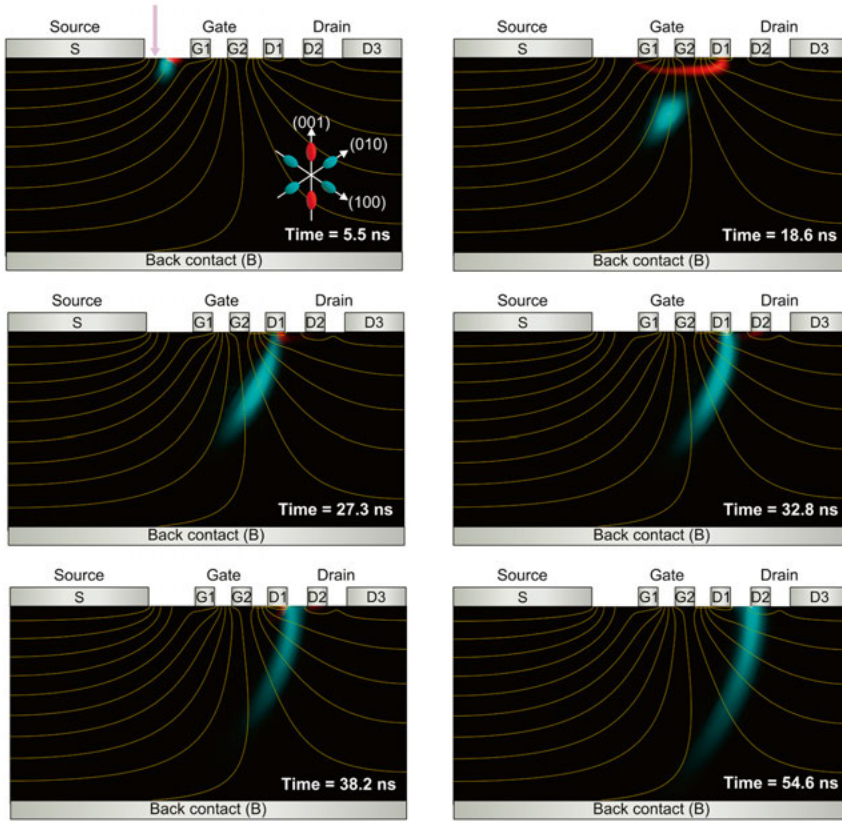


Figure 29. The electron transport in a sample with a thickness of $490 \mu\text{m}$ at different time instances. The source voltage is $V_S = -7 \text{ V}$, gate voltages $V_{G1} = -5 \text{ V}$ and $V_{G2} = -2.4 \text{ V}$ and the back voltage $V_B = -2.4 \text{ V}$. All are referenced to the drain contacts, which are connected to ground.

From these results, it is seen that after 5.5 ns two type of electrons lie closely to the surface and the source contact. The electrons from the (001) valleys (red color) move along the sample surface under the gate contacts and the electrons from the (010) and (100) valleys (turquoise color) move into the sample. At 18.6 ns, the electrons from the (001) valleys are extracted at the

left drain contact (D1) and at 27.3 ns most of them have been extracted. At 54.6 ns, the electrons from the (010) and (100) valleys are extracted at D2. The induced currents at the left drain (D1) and middle drain (D2) contacts as functions of time and left gate voltage (V_{G1}) are shown in Figure 30.

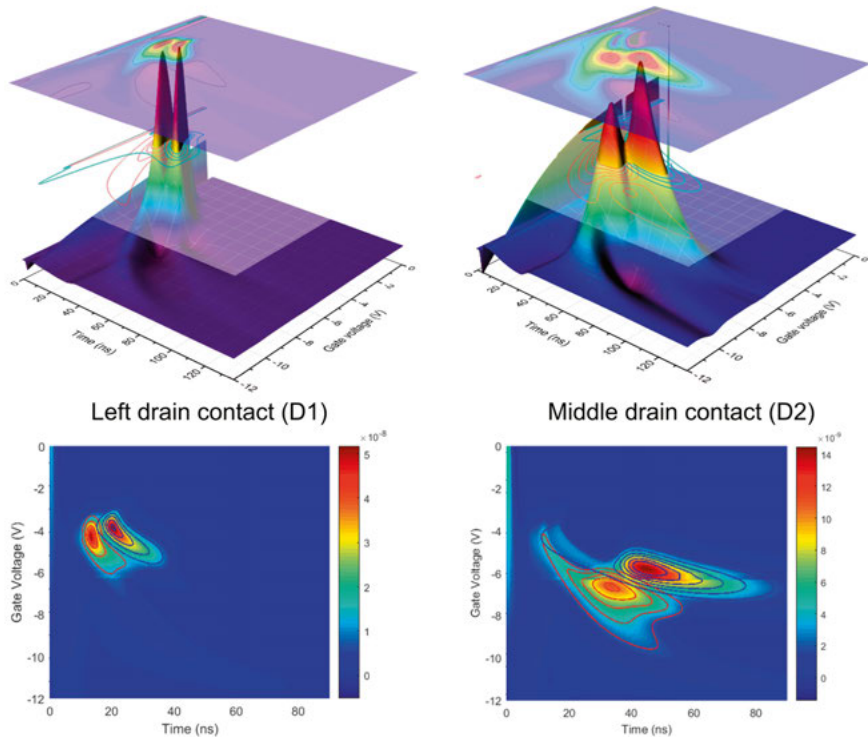


Figure 30. The induced current through D1 (left) and D2 (right), where the red color represents the electrons from the (001) valleys and the turquoise color represents the electrons from the (010) and (100) valleys. These results were achieved with a simulation performed on a sample with a thickness of $490 \mu\text{m}$, a source voltage $V_s = -7 \text{ V}$, right gate voltage $V_{G2} = -2.4 \text{ V}$, back voltage $V_B = -2.4 \text{ V}$ and a left gate voltage (V_{G1}) between -12 and 0 V . The currents induced through D1 and D2 differ more than one magnitude.

These results show that when applying a voltage of -4 V over the left gate contact, two different current peaks are observed through D1. They occur at $\sim 13 \text{ ns}$ by the electrons in (001) valleys and at $\sim 21 \text{ ns}$ by the electrons in (010) and (100) valleys. When instead applying a voltage of -5.6 V , a current peak caused by the electrons from the (010) and (100) valleys can be observed through D2 at 45 ns . An applied voltage of -6.6 V causes the electrons from the (001) valleys to generate a current peak through the same contact at 34 ns .

This simulation showed that it with different voltages were possible to control the type of electrons transmitted. It also indicated a possibility of controlling the information through which of the two types of electrons that were affected. It is however possible to create a third type of electron as well if applying the electric field in a different direction or by applying a magnetic field perpendicular to the electric field.

5.5.2. Experiment

The measurement setup was similar to that described in section 5.2.1. A passively Q-switched UV laser with FWHM pulses of 800 ps and a wavelength of 213 nm at a repetition rate of 300 Hz was used. The photon energy was above bandgap ($h\nu = 5.82 \text{ eV} > E_g = 5.47 \text{ eV}$) and a line near the edge of the source contact was illuminated in order to generate electron-hole pairs. For suitably chosen bias voltages at the source, gate and back contacts, the electrons will under the influence of an electric field drift towards the drain contacts. The drain contacts were held at ground potential and the induced current is given by the Shockley-Ramo theorem [66, 67]. With the chosen geometry, currents were only induced at the contacts when charges move in close proximity to these. The holes were rapidly collected at the source electrode and their contribution to the drain current was negligible.

The transistors were made using SC-CVD samples synthesized under conditions of high purity by Element Six Ltd. The samples were $4.5 \times 4.5 \text{ mm}$ with thicknesses in the range of 390 to 510 μm and the influence of ionized impurity scattering was minimized by selecting the purest CVD diamond samples available. The concentration of nitrogen impurities was by EPR determined to be below 10^{13} cm^{-3} in all samples and the concentration of charged impurities was less than 10^{10} cm^{-3} [68]. A 30 nm thick Al_2O_3 layer was as the gate oxide and surface passivation layer deposited on the top (100) surface of the diamond using atomic layer deposition. The source, gate and drain contacts of Ti/Al were evaporated with a 10/250 nm thickness together with lithographic techniques to make a pattern between the oxide layer and the source and drain contacts. Buffered Hydrogen Fluoride (HF) was used for etching the Al_2O_3 layer. The back surface (100) was similarly metalized by Ti/Al covering the entire surface. A schematic of the transistors is shown in Figure 31 (right).

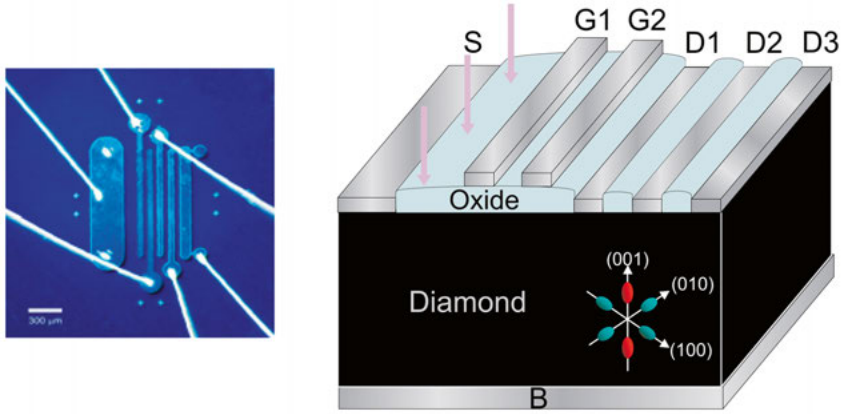


Figure 31. The diamond sample with its electrodes (left) and a schematic of the transistor (right) used in the experiment.

Results and conclusion

The currents induced through contact D1 and D2 as functions of left gate voltage are shown in Figure 32.

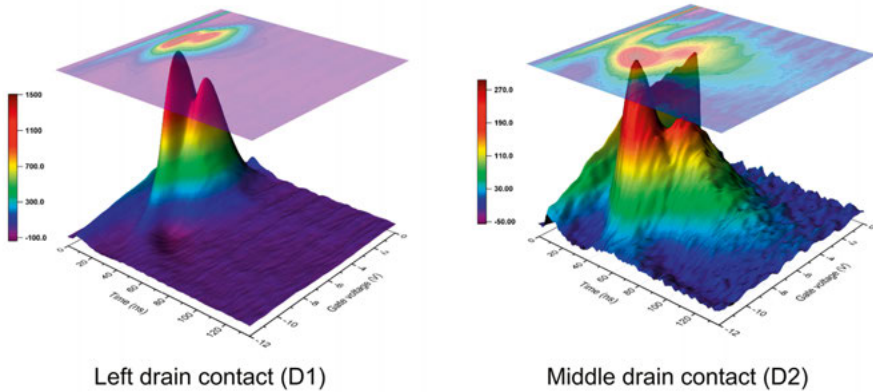


Figure 32. The experimental results of the currents induced through D1 (left) and D2 (right) measured on an SC-CVD diamond with a thickness of $490\ \mu\text{m}$ at $V_S = -7\ \text{V}$, $V_{G2} = -2.4\ \text{V}$, $V_B = -2.4\ \text{V}$ and $V_{G1} = -12\ \text{V}$ to $0\ \text{V}$.

Two separate peaks are clearly seen with different arrival times for different left-gate voltages. For D1, the first peak is observed at $13\ \text{ns}$ and $5.4\ \text{V}$ and the second peak at $21\ \text{ns}$ and $4\ \text{V}$. For D2, the first peak is observed at $31\ \text{ns}$ and $8\ \text{V}$ and the second peak at $45\ \text{ns}$ and $6\ \text{V}$. These experimental results are similar to those from the simulation, and thus we know that these peaks can be attributed to electrons in different states of valley polarization arriving at the contacts.

5.6. Summary

Our findings have shown the existence of valley polarization in diamond and explained how this can occur. This was followed by a further investigation of different perspectives such as the relaxation time and the mechanisms of valley polarization at low temperatures. The latter was done to see the dominant scattering mechanisms and whether the valley polarization was affected by the application of a magnetic field. This gave interesting explanations as to what causes these effects, but also a confirmation that it is possible to create a valley-transistor based on diamond. This was in the end realized with a double-gate transistor. The simulation and the experiment agreed well with each other and an all-electric control of valley states was achieved. Enabling full control of these polarization states requires further experiments, but together with the unique properties of diamond we are getting closer towards valleytronic applications.

6. Conclusion

The purpose of this research was to investigate the electron charge transport properties in diamond at low temperatures. Studying the material at these temperatures where the phonon scattering rate is low, leads to a better understanding of its electronic properties. This is crucial in determining how and if it is possible to use diamond in electronic devices. Our group has through the analysis of carrier behavior previously discovered the two phenomena Negative Differential Mobility (NDM) and valley polarization occurring in diamond. They are both based on the electrons' non-equilibrium valley populations.

There are today devices available utilizing an NDM effect, mainly to create oscillators or amplifiers working at microwave frequency, such as tunnel diodes or Gunn diodes. Simulations presented in this thesis used a model based on observed NDM results and gave promising indications that it is possible to create a Transferred-Electron Oscillator (TEO) based on diamond. The parameters for creating such a device were also found.

The repopulation model was created as an improvement to this model and was proved to be in good agreement with Time-of-Flight (ToF) measurements. Oscillations were achieved in a TEO device at a limited temperature and voltage range. When fabricated based on a diamond sample, it was found to oscillate even outside the range of where the NDM effect had previously been observed. Further investigations are needed in order to fully explain the repopulation of electrons as well as the oscillations occurring in diamond.

Valleytronics use the valley-polarized states to encode information, and thus their stability is of utmost importance. Our group has proven that a relaxation time of up to microseconds or longer at temperatures below 100 K and electric fields below 100 V/cm can be obtained. It has also been found that it is possible to transfer this information across macroscopic distances.

The study of the mechanisms involved in the conduction band transport of valley-polarized electrons was presented at a temperature range of 10 to 80 K for very low electric fields, well below 10 V/cm. At these conditions, carrier heating is involved in the observations of non-ohmic behavior. For the first time ever, the effects of inelastic scattering on free carriers have been observed in a drift velocity measurement. This study has also shown the possibility to obtain values of the momentum relaxation time of valley-polarized electrons.

Magneto-Time-of-Flight (Magneto-ToF) is a new technique, similar to ToF, which can be used for measuring carrier charge transport properties such as velocity and mobility. In addition, Magneto-ToF can also be used for detecting valley-polarized electrons and allows for the study of magnetotransport and the dominant scattering mechanisms at low temperatures. This thesis has described the setup and the theory behind this method and it was concluded that at a temperature of 70 K, acoustic phonon scattering was the dominant electron scattering mechanism in the tested samples.

In an attempt of exploiting the effects of valley polarization in diamond, a valley-transistor was created and both a theoretical and an experimental investigation were performed. Together they proved that it is possible to create a valley-transistor with the structure of a double-gate, where an all-electric control of the valley states is achievable. Enabling a complete control of the valley polarization however requires further research. Together with the unique properties of diamond, these discoveries and the progress made by our group might lead towards valleytronic applications.

7. Summary of papers

This chapter summarizes the seven papers this thesis is based on and presents the author's contributions to them.

Paper I: Magnetotransport study of valley-polarized electrons in synthetic diamond

A new technique called Magneto-Time-of-Flight (Magneto-ToF) that is based on ToF and the Hall Effect is introduced. By applying a magnetic field perpendicular to the electric field it is possible to study the charge transport, magnetoresistivity and to determine the dominant scattering mechanisms. The results show that at a temperature of 70 K acoustic phonon scattering was the dominant electron scattering mechanism in the tested samples.

The author of this thesis has collected and analyzed the data, processed the results and has also been one of the main authors of the manuscript.

Paper II: Investigation of transferred-electron oscillations in diamond

A possibility of making a diamond-based Transferred-Electron Oscillator (TEO) by utilizing the Negative Differential Mobility (NDM) effect at a temperature of 110 K is presented. A simulation based on drift-diffusion, Poisson's equation and on previously performed NDM observations occurring at a temperature range of 100 to 150 K in Single-Crystalline Chemical Vapor Deposition (SC-CVD) diamond is performed. The relationship between electric field and electron drift velocity is established by fitting an analytical expression to the experimental drift velocity data. A TEO device is also simulated in order to map out the parameters that give rise to oscillations with the highest possible amplitude and stability.

The author of this thesis has been the main responsible for planning, executing and analyzing the simulations and has also been the main author of the manuscript.

Paper III: Low temperature conduction-band transport in diamond

A better understanding of the mechanisms involved in the conduction band transport of valley-polarized electrons is achieved by measuring the drift velocities of electrons at a temperature range of 10 to 80 K for very low electric fields, well below 10 V/cm. The results are compared with Monte Carlo (MC)

simulations in order to identify the dominant scattering mechanisms. The effects of carrier heating and inelastic phonon-electron scattering is also discussed. The momentum relaxation rate for electrons with different valley polarization as a function of temperature is presented.

The author of this thesis has participated in the experiments and in internal reviews of the manuscript.

Paper IV: Stability of polarized states for diamond Valleytronics

A continued investigation into the valley-polarized electrons observed in diamond is performed. SC-CVD diamond samples with an impurity concentration lower than 10^{13} cm^{-3} show a relaxation time as long as 300 ns at electric fields below 100 V/cm and temperatures below 100 K. The stability of the valley-polarized electrons is crucial and, if high enough, enables them to be used in valleytronic applications to encode, transport and decode information. By using MC simulations it is found that the stability of the polarized states depends strongly on temperature and electric field due to electron-phonon interaction.

The author of this thesis has participated in the experiments and in internal reviews of the manuscript.

Paper V: Charge Transport Phenomena Unique to Diamond

Electron and hole charge transport is reviewed and observations reveal that electron and hole drift velocities are similarly affected by a change in the electric field at temperatures above 150 K, but fundamentally differently at lower temperatures. This is due to the structural differences in the conduction band and valence band. Two interesting phenomena occurring in diamond are also presented. NDM occurs at temperatures below 150 K and valley-polarized electrons are observed at temperatures below 100 K.

The author of this thesis has participated in internal reviews of the manuscript.

Paper VI: Electrostatic control of valley pseudospin in dual-gate diamond transistors

Simulations as well as experiments for creating a valley-transistor are presented. A diamond-based double-gate field-effect transistor is used and it is found possible to electrostatically control the current and the valley-current separately at a receiving electrode. The results of the simulation agree well with those of the experiment and through the simulation it is confirmed that it is possible to control the valley polarization at different times by only changing the gate voltage.

The author of this thesis has contributed to the experiments, been the main responsible for performing the simulation, has analyzed and discussed the results as well as given valuable input to the manuscript.

Paper VII: Transferred-electron oscillator based on diamond

The first demonstration ever of a practical TEO device based on diamond is presented. Experiments are performed on three different diamond samples at a voltage range of 0 to 30 V and a temperature range of 80 to 330 K. Oscillations are observed and explained by valley repopulation. They are seen even outside the range of where NDM had previously been observed.

The author of this thesis has contributed with the measurements, has been the main responsible for the simulation including its creation, execution and analysis and is also the main author of the manuscript.

8. Suggestions for future work

This chapter gives an idea of what can be researched further in order to expand our understanding of charge carrier transport in diamond and to eventually be able to create electronic devices based on the material.

The investigation and creation of a valley-transistor based on diamond, controlled by two different types of electrons through the application of an electric field, were explained in section 5.5. Full control of the electrons' polarization was achieved by using only an electric field. One aspect that is proposed to be analyzed further is to perform similar experiments, but instead of applying the electric field in $[110]$ direction, it is instead applied in either $[100]$ or $[010]$ direction in an attempt to distinguish a third kind of electron polarization as illustrated in Figure 33.

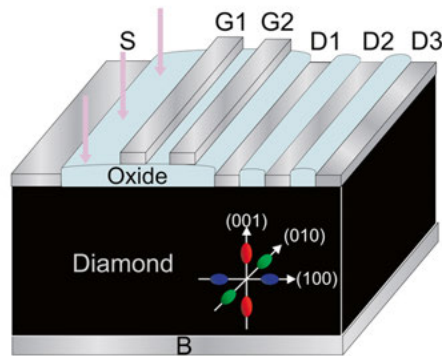


Figure 33. An illustration of a sample and a valleytronics experiment suggested for making it possible to control three types of electron polarizations instead of two.

Through this we would not only get control of another type of electron polarization but it would also allow a higher degree of freedom in the choice of parameters to tweak in an electronic device. This could theoretically lead to three different type of information bits allowing for more complex or more tightly packed (smaller) devices.

Another (but less practical) way forward would be to also utilize a magnetic field in one of the directions instead of only the electric, as this is also a possible approach of generating a third kind of electron.

To improve the accuracy of the simulations of the TEO, ensemble MC simulations should be performed. In these simulations, which can be computationally very demanding, a large ensemble of electrons are followed together with the induced electric field. This type of simulation should give a reasonable accuracy with known microscopic parameters for the electron transport.

To make useful TEO devices it will be necessary to inject carriers electrically through a junction rather than generate them optically. Methods to do this could be investigated, e.g. injection from heavily phosphorous doped diamond.

Acknowledgement

Science, new discoveries and especially aspects of the previously unknown and where no-one else has been before fascinates me. I thrive in the university life and the variety of nationalities in our division has given me the very best opportunities and is something that I am happy to have been part of.

One of the most important people during the course of my PhD studies is of course my main supervisor, Jan Isberg. He has given me good support whenever I have asked for it. He has been invaluable and guided me through tough situations, both emotional and professional. I cannot enough explain how much I would want to express my gratitude for his supervision during my five years as a PhD student at Uppsala University. Thank you Jan for the time as my supervisor.

I would like to thank my second supervisor, Markus Gabrysch, who has always been really thorough in reviewing my work, which has helped me in many ways. I would also like to thank my third supervisor, Saman Majdi, who was appointed last year and who has given me many good ideas, especially when it comes to presenting my data in a clear and interesting way. It has been the best time with both of you as you have not only been my supervisors or colleagues, but also become my friends. You have helped me to fill my knowledge gaps and have made me feel very happy and excited to come to the office. You have always made me feel welcome and helped me to integrate not only in the group but also in the division. Thank you both for everything.

I would like to thank my mentor and the head of the division, Mats Leijon, for giving me the opportunity to be part of this division and extend my knowledge. Thank you for making me feel welcome. I would like to thank Thomas Götschl who has always helped me with all my computer problems, both big and small. I would like to thank the administration who takes care of the economic aspects of our division.

I would like to thank my friends in the electricity division. Thank you for all the enjoyable lunches we have had. It has been fun and nice to get to know you. I would also like to thank all my friends for sharing the nice moments we have had outside working hours. This had made me feel warm and never lonely in this cold country. I know that we will stay friends.

I would like to thank my family, Suntornwipat, who has always supported me no matter what choices I have made. I am really happy to be your daughter as well as sister. For every hard time that I have had and every difficult decision that I have had to make, I am really thankful for the support you have given me. Thank you so much.

I would like to thank the Hägglund family. Thank you for everything, as you already from the beginning made me feel like I am part of the family. I do not have enough words to say how wonderful you have been. I have learned a lot about Swedish culture and language from you all. Thank you again and again.

Finally, I left the last part to thank the most important person in my life, my husband, Joel Hägglund. My words will never be enough in explaining how deeply grateful and happy I am to be with you. You are a great supporter and energy tank for me at all times, no matter what has happened. You have helped me get through both good and bad times and I would like to give you big credits and thanks for making me get this far and for having helped me get through my PhD studies. Thank you so much Joel - my best friend, great husband and father of our daughter, Evelyn.

♡ I love you both so much ♡

Summary in Swedish

Det är diamants optiska egenskaper som särskiljer den från andra ädelstenar och tillsammans med dess hårdhet (tio på Mohs skala) gör det materialet synnerligen attraktivt. Det används inom smyckesindustrin samt för borrar, skärning och slipning. Diamant är också ett material med ett mycket stort bandgap på 5.47 eV i rumstemperatur och med flertalet otroliga egenskaper. Materialet kan i rumstemperatur leda värme tio gånger bättre än koppar, har en hög genombrottsspänning och har högst total mobilitet av alla kända halvledare. Diamant är därför en god kandidat till att kunna vara ett aktivt material i kraftelektroniska produkter.

Naturliga diamanter är väldigt sällsynta och dyrbara. De skapas i en oerhört lång process under en väldigt hög temperatur och ett högt tryck. Det finns två huvudsakliga metoder för att syntetiskt framställa diamant, där den ena försöker efterlikna dessa naturliga processer genom ett högt tryck och en hög temperatur (HPHT) och den andra använder en metod som kallas kemisk ångdeponering (CVD). HPHT var den metod som utvecklades först, men senare visade sig CVD orsaka färre oönskade förskjutningar och ge en lägre koncentration av föroreningar. CVD har kontinuerligt förbättrats för att nu kunna skapa enkristallina, Single-Crystalline (SC), diamanter med en mycket hög renhet. Det är nu därför möjligt att på allvar analysera och studera diamants elektriska och fysikaliska egenskaper. Det är högst troligt att detta kommer bana väg för en ny generation av elektroniska komponenter baserade på diamant.

Under de senaste åren har vår forskargrupp upptäckt två nya fenomen som förekommer i diamant, nämligen Negativ Differential Mobilitet (NDM) samt grupperingar av olika elektronpolarisation (electron valley polarization). Denna doktorsavhandling ger en kort bakgrund till dessa två fenomen. Här ingår även resultat från undersökningar av hur man kan dra fördel av förekomsten av NDM och hur egenskapen kan användas för att simulera, men även framställa en Gunndiod (Transferred-Electron Oscillator, TEO). Två olika simuleringsmodeller har skapats, där den första är baserad på upptäckten av NDM-egenskaperna och den andra baseras på elektronernas omgruppering (valley repopulation). De erhållna resultaten från den första simuleringsmodellen visar att det bör vara möjligt att skapa en Gunndiod men ger också en

fingervisning av vilka de relevanta parametrarna är och deras justeringsmån. Den andra simuleringsmodellen behöver förbättras.

Stabiliteten hos elektronerna som polariserar sig i olika grupper (valley-polarized electrons) har också undersökts. Vid temperaturer under 100 K och elektriska fält under 100 V/cm kan relaxationstiden vara mycket lång, till och med mikrosekunder och det är därför möjligt att polarisationen skulle kunna användas för att koda, transportera och avkoda information. För att kunna använda diamant i dessa tillämpningar (valleytronics) krävs låga temperaturer.

En studie av de mekanismer som påverkar transporten av de polariserade elektronerna i ledningsbandet är gjord inom ett temperaturområde mellan 10 och 80 K för mycket små elektriska fält, lägre än 10 V/cm. Vid dessa förhållanden påverkar laddningsbärarnas värmeeffekter, vilket kan observeras genom ett icke-ohmskt beteende i deras mobilitet. Effekten av de icke-elastiska krockar (scattering) som sker med fria laddningsbärare har tidigare aldrig kunnat direkt observeras för någon halvledare enbart genom experiment som syftar till att mäta deras genomsnittliga hastighet (drift velocity). Denna studie har visat det möjligt att erhålla relaxationstiden för polariserade elektroner.

Time-of-Flight (ToF) är en teknik som kan användas för att studera laddningsbärarnas transportförmåga genom att mäta deras genomsnittliga hastighet samt mobilitet men som även kan användas för att studera elektronernas polarisation. ToF, som också kallas för Transient Current Technique (TCT), är speciellt en kraftfull metod för att studera de elektriska egenskaperna hos halvledare med hög resistivitet och låg koncentration av laddningsbärare. Denna teknik är överlägsen Hall-effektmätningar för material med stora bandgap, t.ex. diamant. Elektron-hål-par kan skapas med olika metoder, men i vår forskargrups uppsättning så används en laser som genererar korta pulser. De fria laddningsbärarna transporteras med hjälp av ett genererat elektriskt fält och den inducerade strömmen mäts vid en elektrod. I denna avhandling presenteras den nya tekniken Magneto-ToF, vilken är en modifiering av den ursprungliga ToF, där ett magnetfält genereras vinkelrätt mot det elektriska fältet. Hall-effekten ger då upphov till icke-isotropa tillskott i mobilitetsvektorn och möjliggör observation av en tredje polarisation. Denna nya metod gör det möjligt att studera laddningsbärarnas transportegenskaper, deras magnetoresistivitet samt de dominerande mekanismer som orsakar laddningsbärarnas krockar/spridning och därför begränsar deras genomsnittliga hastighet.

Efter att ha fått en bättre förståelse för den elektronpolarisation som kan visa sig i diamant har en transistor som möjliggör olika polarisationstillstånd tillverkats. En teoretisk och experimentell utredning har gjorts och tillsammans visade det sig att det är möjligt att skapa en sådan transistor med två styrelektroder (gates) där en helt elektrisk kontroll av elektronernas polarisation uppnåddes. Att möjliggöra fullständig kontroll över denna polarisation

kräver dock ytterligare experiment. Tillsammans med diamants unika egenskaper leder dessa upptäckter och de framsteg som gjorts i vår forskargrupp stadigt framåt till att så småningom kunna skapa komponenter baserade på elektronernas polarisation istället för deras elektriska laddning.

Appendix – Repopulation model evaluation

This appendix gives details about the relationship between the carrier temperatures and the electric field which was found with a least square's fit of Monte Carlo (MC) simulation results. Evaluation of the repopulation model was performed by comparing this with data from Time-of-Flight (ToF) measurements.

The relationship between the carrier temperatures and the electric field is seen in Figure 34, which shows results from our study presented in **Paper III** and **Paper IV**. MC simulations were performed for a simplified conduction band structure, adequate for moderate electric fields, consisting of six parabolic but anisotropic valleys with $m_l^* = 1.56m_0$ and $m_t^* = 0.28m_0$ [14]. The six band minima are located at 76% of the BZ boundary in the $\{100\}$ directions with ellipsoidal constant energy surfaces. Acoustic phonon intervalley scattering was treated through inelastic deformation-potential interaction with a deformation potential (D_A) equal to 11.5 eV [37] and intervalley scattering was included through f - and g - scattering deformation potential interactions, $D_f = D_g = 4 \times 10^8$ eV/cm [22]. The longitudinal acoustic velocity (v_l) is equal to 17.52 km/s [39] and the transverse acoustic velocity (v_t) is equal to 12.82 km/s [39] at a temperature of 110 K. It was assumed that the constant transition phonon energies are $\hbar\omega_f = 120$ meV and $\hbar\omega_g = 165$ meV.

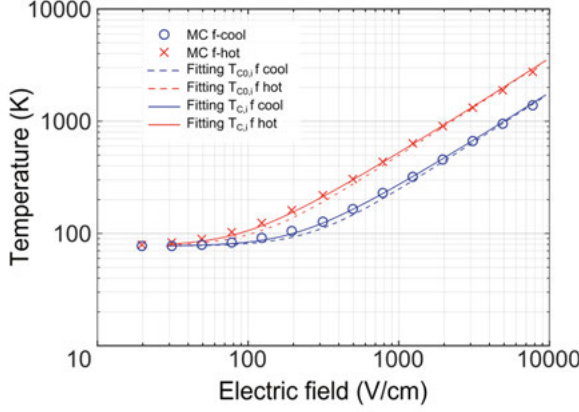


Figure 34. The carrier temperatures as function of the electric field found with an MC simulation using deformation potentials $D_A = 11.5$ eV and $D_f = 4 \times 10^8$ eV/cm. The lines indicate the least square's fits.

A semi-empirical expression was with an iterative method fitted to the results in order to find the electron and hole temperatures and their dependence on the electric field strength:

$$T_c^p = \left(T_L T_{c0,p}^{1.31} + \frac{k_{MC}}{\sqrt{T_L}} \mu_{300,p} |E|^2 \right)^{1/2.31} \quad (\text{A.1})$$

$$T_c^{ni} = \left(T_L T_{c0,ni}^{1.31} + \frac{k_{MC}}{\sqrt{T_L}} (\mu_{300,ni,xx} E_x^2 + \mu_{300,ni,yy} E_y^2 + \mu_{300,ni,zz} E_z^2) \right)^{1/2.31} \quad (\text{A.2})$$

where

$$T_{c0,p} = \left(T_L^{2.31} + \frac{k_{MC}}{\sqrt{T_L}} \mu_{300,p} |E|^2 \right)^{1/2.31} \quad (\text{A.3})$$

$$T_{c0,ni} = \left(T_L^{2.31} + \frac{k_{MC}}{\sqrt{T_L}} (\mu_{300,ni,xx} E_x^2 + \mu_{300,ni,yy} E_y^2 + \mu_{300,ni,zz} E_z^2) \right)^{1/2.31} \quad (\text{A.4})$$

k_{MC} is the free parameter obtained from fitting the results to temperature and $\mu_{300,p}$ is the isotropic hole mobility at a temperature of 300 K. $\mu_{300,ni,\alpha\alpha}$ are the non-isotropic electron mobilities at a temperature of 300 K which differ depending on the direction of the applied electric field. E_x , E_y and E_z are the components of the electric field along the x -, y - and z -axis respectively.

The continuity equations become

$$\frac{\partial p}{\partial t} - \mu_p \left(\frac{\partial}{\partial x_\alpha} \left(p \frac{\partial}{\partial x_\alpha} \Phi \right) + \frac{k T_c^p}{q} \left(\frac{\partial^2}{\partial x_\alpha^2} p \right) - \frac{k}{q} \frac{\partial}{\partial x_\alpha} \left(p \frac{\partial}{\partial x_\alpha} T_c^p \right) \right) = g_p - r_p \quad (\text{A.5})$$

$$\frac{\partial n_i}{\partial t} + (\tilde{\mu}_{ni})_{\alpha\beta} \left[\frac{\partial}{\partial x_\alpha} \left(n_i \frac{\partial}{\partial x_\beta} \Phi \right) - \frac{k T_c^{ni}}{q} \frac{\partial}{\partial x_\alpha} \frac{\partial}{\partial x_\beta} n_i - \frac{k}{q} \frac{\partial}{\partial x_\alpha} \left(n_i \frac{\partial}{\partial x_\beta} T_c^{ni} \right) \right] = g_{ni} - r_{ni} \quad (\text{A.6})$$

and we assume the same electron and hole generation and recombination rates as was mentioned in section 2.4.2.

The expression for the scattering time in and out of a pair of valleys on an orthogonal axis in k -space was found by fitting the results of the relaxation time versus the electric field at a temperature range of 77 to 300 K (**Paper IV**) and can be seen in Figure 35. The fit is separated into two parts where τ_0 is the scattering time between the valleys that does not depend on the electric field and $\tau_{p0w,i}$ is the one that does.

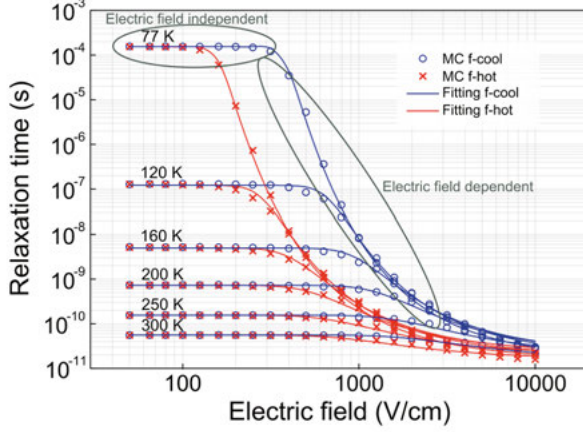


Figure 35. The results fitted to an MC simulation of the relaxation time's dependence on the electric field at a temperature range of 77 to 300 K.

The scattering time in and out of conduction band valley i can be found from

$$\tau_{ni} = \left(\tau_0^{-\beta} + \tau_{Pow,ni}^{-\beta} \right)^{\frac{1}{\beta}} \quad (\text{A.7})$$

where

$$\tau_0 = a \exp\left(\frac{b}{T_L}\right), \quad (\text{A.8})$$

$$\tau_{Pow,ni} = c \sqrt{T_L/T_{77}} \exp\left(\frac{d}{\sqrt{\frac{E_x^2}{m_{ni,xx}} + \frac{E_y^2}{m_{ni,yy}} + \frac{E_z^2}{m_{ni,zz}}}} \right), \quad (\text{A.9})$$

were found to be good fits with $a = 3.33 \times 10^{-13}$ s, $b = 1537$ K, $c = 1.6 \times 10^{-11}$ s, $d = 4947.3$ V/cm $\sqrt{\text{kg}}$, $\beta = 0.75$ and $T_{77} = 77$ K. m_{xx} , m_{yy} and m_{zz} are the electron effective masses which depend on the valley i and can be either m_l^* or m_t^* .

The TEO was implemented in the same way as for the NDM Model (Figure 14). The constants used in the model were $I = 1.776 \times 10^{17}$ cm $^{-2}$ s $^{-1}$, $\kappa = 50$ cm $^{-1}$, $\epsilon_r = 5.7$, $T = 110$ K, $E_g = 5.47$ eV and $\tau_n = \tau_p = 10$ μ s, $\mu_{300,p} = 3000$ cm 2 /Vs, $\mu_{300,t} = 580$ cm 2 /Vs, $\mu_{300,l} = 3210$ cm 2 /Vs, $m_l^* = 1.56m_0$ and $m_t^* = 0.28m_0$.

Firstly, the simulation results were compared with standard ToF measurements performed with a non-continuous light source. This was performed for three different temperatures and two different voltages. At a voltage of 10 V and a temperature of 78 K two different types of electrons were observed, but NDM was most pronounced at a temperature of 110 K. At a temperature of 300 K only one type of electron was observed. Figure 36 shows this comparison with the current as a function of time at the temperatures 78, 110 and 300 K and the voltages 10 and 30 V.

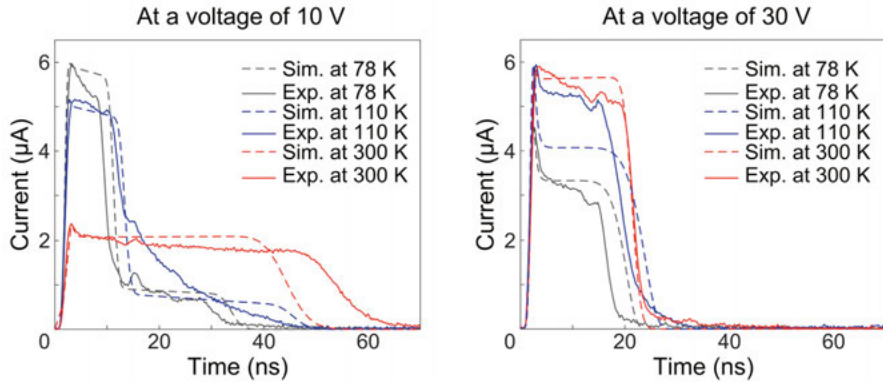


Figure 36. A comparison of the current transients as functions of time between the drift-diffusion simulations and the ToF measurements performed on a sample with a thickness of 307 μm , temperatures of 78, 110 and 300 K and an applied voltage of 10 V (left) and 30 V (right). The constants are $a = 3.33 \times 10^{-13}$ s, $b = 1537$ K, $c = 1.6 \times 10^{-11}$ s, $d = 4947.3$ V/cm $\sqrt{\text{kg}}$, $\beta = 0.75$ and $k_{MC} = 4.6 \times 10^{-3}$.

At a temperature of 300 K and a voltage of 30 V, the results seem to agree well. At a temperature of 110 K and a voltage of 10 V, the agreement is however poor and to explain our experiment results for all parameter ranges the model was not considered good enough. This lack of correlation might be because of a lower scattering factor between the valleys in the simulation than in the experiment. The constants that affect the scattering factor are a , b , c , d , β and k_{MC} .

A better fit was found with $a = 3.33 \times 10^{-13}$ s, $b = 1200$ K, $c = 1.6 \times 10^{-11}$ s, $d = 3850$ V/cm $\sqrt{\text{kg}}$, $\beta = 0.75$ and $k_{MC} = 1.5 \times 10^{-3}$. A new comparison performed is shown in Figure 37.

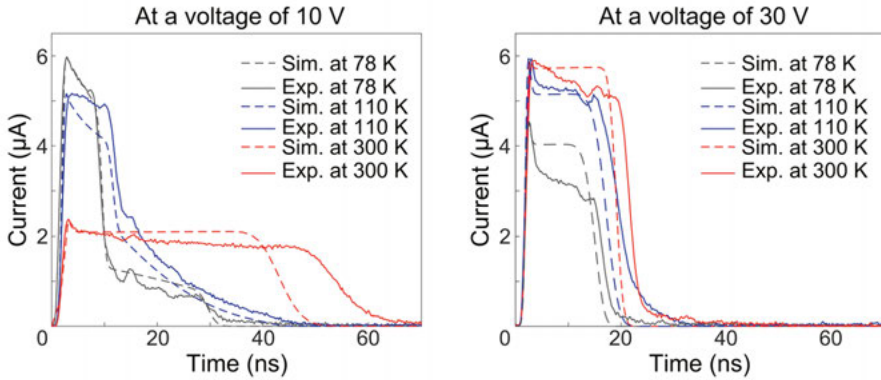


Figure 37. A comparison of the current transients as functions of time between the drift-diffusion simulations and the ToF measurements performed on a sample with a thickness of 307 μm , a temperature of 78, 110 and 300 K and an applied voltage of 10 (left) and 30 V (right). The constant are $a = 3.33 \times 10^{-13}$ s, $b = 1200$ K, $c = 1.6 \times 10^{-11}$ s, $d = 3850$ V/cm $\sqrt{\text{kg}}$, $\beta = 0.75$ and $k_{MC} = 1.5 \times 10^{-3}$.

The new constants were seen to give a better fit for all ranges of temperature and voltage, especially at 110 K and 10 V. The changed values however affect the temperatures of the electrons and also the electric field. Since the relaxation time depends on the electric field, this is also changed and seen in Figure 38.

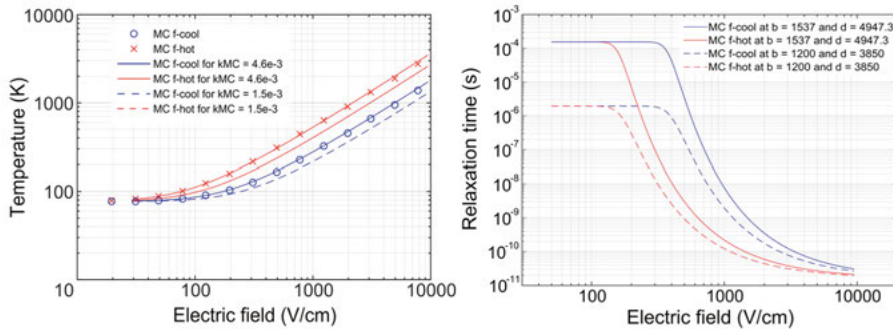


Figure 38. Comparison of the carrier temperatures using $k_{MC} = 4.6 \times 10^{-3}$ and $k_{MC} = 1.5 \times 10^{-3}$ (left). Comparison of the relaxation times using $b = 1200$ K, $d = 3850$ V/cm $\sqrt{\text{kg}}$ and $b = 1537$ K, $d = 4947.3$ V/cm $\sqrt{\text{kg}}$, both at a temperature of 77 K and as a function of the electric field (right). The simulation results are also presented, with $D_A = 11.5$ eV and $D_f = 4 \times 10^8$ eV/cm.

The relaxation time's dependence on the electric field at a temperature range of 77 to 300 K is shown in Figure 39.

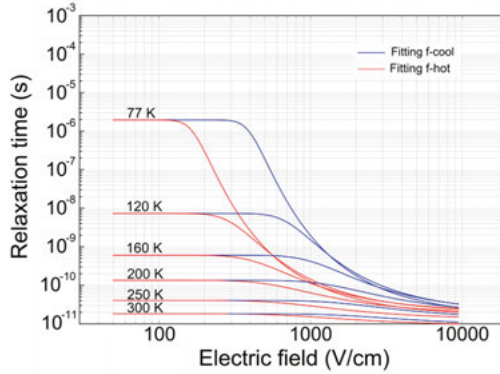


Figure 39. The relaxation time as a function of the electric field at a temperature range of 77 to 300 K with $a = 3.33 \times 10^{-13}$ s, $b = 1200$ K, $c = 1.6 \times 10^{-11}$ s, $d = 3850$ V/cm $\sqrt{\text{kg}}$ and $\beta = 0.75$.

The drift velocities as functions of the electric field obtained for a sample with a thickness of 307 μm are shown in Figure 40 for the temperatures 130, 150 and 300 K. They show good agreement at all temperatures and were also compared for samples with thicknesses of 390 and 420 μm . These comparisons gave similar results, but are not presented here. The rather good agreement for the current transients and the drift velocities as functions of the electric field give credibility to the repopulation model.

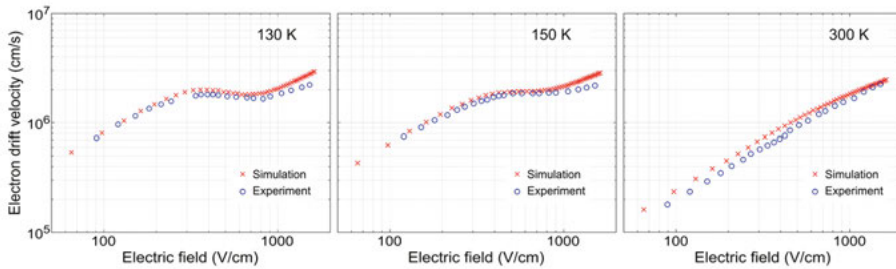


Figure 40. Comparison of the drift velocity as a function of the electric field between the simulation and the experimental results performed on a sample with thickness 307 μm at the temperatures 130, 150 and 300 K.

Bibliography

1. Seidenberg P (1997) From Germanium to Silicon, A History of Change in the Technology of the Semiconductors. *IEEE Cent Hist Electr Eng* 35–74
2. Chikuni E, Inya Okoro O, Khan MT (2008) *Concise Higher Electrical Engineering*. Juta and Company Ltd
3. Tolbert LM, Ozpineci B, Islam SK, Chinthavali MS Wide bandgap semiconductors for utility applications. *semiconductors* 1:3
4. Shenai K, Scott RS, Baliga BJ (1989) Optimum semiconductors for high-power electronics. *IEEE Trans Electron Devices* 36:1811–1823. doi: 10.1109/16.34247
5. Abad G (2017) *Power Electronics and Electric Drives for Traction Applications - Gonzalo Abad*. John Wiley&Sons, Ltd.
6. Isberg J, Hammersberg J, Johansson E, et al (2002) High Carrier Mobility in Single-Crystal Plasma-Deposited Diamond. *Science* 297:1670–1672. doi: 10.1126/science.1074374
7. Chow TP, Omura I, Higashiwaki M, et al (2017) Smart Power Devices and ICs Using GaAs and Wide and Extreme Bandgap Semiconductors. *IEEE Trans Electron Devices* 64:856–873. doi: 10.1109/TED.2017.2653759
8. Sussmann RS (2009) *CVD Diamond for Electronic Devices and Sensors*. John Wiley & Sons, Ltd
9. Isberg J, Gabrysch M, Majdi S, Twitchen DJ (2012) Negative mobility in diamond. *Appl Phys Lett* 100:172103
10. Isberg J, Gabrysch M, Hammersberg J, et al (2013) Generation, transport and detection of valley-polarized electrons in diamond. *Nat Mater* 12:760–764
11. Pan LS, Kania DR (1995) *Diamond: Electronic Properties and Applications*. Kluwer Academic Publishers
12. Ashcroft NW, Mermin (1976) *Solid State Physics*. Saunders Colleges Publishing
13. Dean PJ, Lightowlers EC, Wight DR (1965) Intrinsic and extrinsic recombination radiation from natural and synthetic aluminum-doped diamond. *Phys Rev* 140:A352–A369
14. Naka N, Fukai K, Handa Y, Akimoto I (2013) Direct measurement via cyclotron resonance of the carrier effective masses in pristine diamond. *Phys Rev B* 88:035205
15. Löfas H, Grigoriev A, Isberg J, Ahuja R (2011) Effective masses and electronic structure of diamond including electron correlation effects in first principles calculations using the GW-approximation. *AIP Adv* 1:032139

16. Pavone P, Karch K, Schutt O, et al (1993) Ab initio lattice dynamics of diamond. *Phys Rev B Condens Matter* 48:3156–3163
17. Kittel C (1996) *Introduction to Solid State Physics*, 7th ed. John Wiley & Sons, Inc.
18. Lundstrom M *Fundamentals of Carrier Transport*, Second Edition. Cambridge University Press
19. Sze SM, Ng KK *Physics of Semiconductor Devices*, 3rd Edition. John Wiley & Sons, Inc.
20. Shukla MM, Padial NT (1973) A Calculation of the Debye Characteristic Temperature of Cubic Crystals. *Rev Bras Física* 3:
21. Schwoerer-Böhning M, Macrander AT, Arms DA (1998) Phonon dispersion of diamond measured by inelastic X-ray scattering. *Phys Rev Lett* 80:5572–5575
22. Hammersberg J, Majdi S, Kovi KK, et al (2014) Stability of polarized states for diamond valleytronics. *Appl Phys Lett* 104:232105
23. Pomorski M, Berdermann E, Caragheorghopol A, et al (2006) Development of single-crystal CVD-diamond detectors for spectroscopy and timing. *Phys Status Solidi Appl Mater Sci* 203:3152–3160
24. Ferry DK (1975) High-field transport in wide-band-gap semiconductors. *Phys Rev B* 12:2361–2369. doi: 10.1103/PhysRevB.12.2361
25. Sze SM, Lee MK (2012) *Semiconductor Devices: Physics and Technology*, 3rd Edition. John Wiley & Sons, Inc.
26. Li Z, Kraner HW (1993) Modeling and simulation of charge collection properties for neutron irradiated silicon detectors. *Nucl Phys B - Proc Suppl* 32:398–409. doi: 10.1016/0920-5632(93)90052-8
27. Sze SM (2002) *Semiconductor Devices: Physics and Technology*, 2nd ed. John Wiley & Sons, Inc.
28. Gabrysch M (2010) *Charge Transport in Single-crystalline CVD Diamond*. Acta Univ Ups
29. Levinshtein ME, Rumyantsev SL, Shur M (1996) *Handbook series on semiconductor parameters*. 1. Si, Ge, C (diamond), GaAs, GaP, GaSb, InAs, InP, InSb. World Scientific Publishing Company, Incorporated
30. Borst TH, Weis O (1996) Boron-Doped Homoepitaxial Diamond Layers: Fabrication, Characterization, and Electronic Applications. *Phys Status Solidi A* 154:423–444. doi: 10.1002/pssa.2211540130
31. Isberg J, Lindblom A, Tajani A, Twitchen D (2005) Temperature dependence of hole drift mobility in high-purity single-crystal CVD diamond. *Phys Status Solidi A* 202:2194–2198
32. Redfield AG (1954) Electronic Hall Effect in Diamond. *Phys Rev* 94:526–537. doi: 10.1103/PhysRev.94.526
33. Austin IG, Wolfe R (1956) Electrical and Optical Properties of a Semiconducting Diamond. *Proc Phys Soc Sect B* 69:329
34. Klick CC, Maurer RJ (1951) The Mobility of Electrons in Diamond. *Phys Rev* 81:124–130. doi: 10.1103/PhysRev.81.124

35. Gabrysch M, Majdi S, Twitchen DJ, Isberg J (2011) Electron and hole drift velocity in chemical vapor deposition diamond. *J Appl Phys* 109:063719
36. Majdi S, Kovi KK, Hammersberg J, Isberg J (2013) Hole transport in single crystal synthetic diamond at low temperatures. *Appl Phys Lett* 102:152113–152113
37. Majdi S, Gabrysch M, Kovi KK, et al (2016) Low temperature conduction-band transport in diamond. *Appl Phys Lett* 109:162106
38. Willatzen M, Cardona M, Christensen NE (1994) Linear muffin-tin-orbital and k-midtp calculations of effective masses and band structure of semiconducting diamond. *Phys Rev B Condens Matter* 50:18054–18059
39. Koizumi S, Nebel CE, Nesladek M (2008) *Physics and Applications of CVD Diamond*. Wiley-VCH Verlag GmbH & Co. KGaA
40. Gunn JB (1963) Microwave oscillations of current in III-V semiconductors. *Solid State Commun* 1:88–91
41. Allen JW, Shyam M, Pearson GL (1966) Gunn oscillation in Indium Arsenide. *Appl Phys Lett* 9:39–41. doi: 10.1063/1.1754591
42. Ludwig GW, Halsted RE, Even M (1966) Current saturation and instability in CdTe and ZnSe. *IEEE Trans Electron Devices* ED-13:671–672. doi: 10.1109/T-ED.1966.15763
43. Oliver MR, Foyt AG (1967) The Gunn effect in n-CdTe. *IEEE Trans Electron Devices* 14:617–618. doi: 10.1109/T-ED.1967.16018
44. Ng KK (2002) *Complete Guide to Semiconductor Devices*. John Wiley & Sons, Inc.
45. Suntornwipat N, Majdi S, Gabrysch M, Isberg J (2016) Investigation of transferred-electron oscillations in diamond. *Appl Phys Lett* 108:212104. doi: 10.1063/1.4952766
46. Nava F, Canali C, Jacoboni C, et al (1980) Electron effective masses and lattice scattering in natural diamond. *Solid State Commun* 33:475–477
47. Pernot J, Tavares C, Gheeraert E, et al (2006) Hall electron mobility in diamond. *Appl Phys Lett* 89:122111
48. Clark CD, Dean PJ, Harris PV (1964) Intrinsic edge absorption in diamond. *Proc R Soc Lond Ser Math Phys Sci* 277:312. doi: 10.1098/rspa.1964.0025
49. Murakami S, Nagaosa N, Zhang S-C (2003) Dissipationless Quantum Spin Current at Room Temperature. *Science* 301:1348. doi: 10.1126/science.1087128
50. Mak KF, He K, Shan J, Heinz TF (2012) Control of valley polarization in monolayer MoS₂ by optical helicity. *Nat Nano* 7:494–498. doi: 10.1038/nnano.2012.96
51. Takashina K, Ono Y, Fujiwara A, et al (2006) Valley polarization in Si(100) at zero magnetic field. *Phys Rev Lett* 96:236801
52. Zeng H, Dai J, Yao W, et al (2012) Valley polarization in MoS₂ monolayers by optical pumping. *Nat Nano* 7:490–493. doi: 10.1038/nnano.2012.95
53. Zhu Z, Collaudin A, Fauque B, et al (2012) Field-induced polarization of Dirac valleys in bismuth. *Nat Phys* 8:89–94. doi: 10.1038/nphys2111

54. Cao T, Wang G, Han W, et al (2012) Valley-selective circular dichroism of monolayer molybdenum disulphide. *Nat Commun* 3:887. doi: 10.1038/ncomms1882
55. Gunawan O, Shkolnikov YP, Vakili K, et al (2006) Valley Susceptibility of an Interacting Two-Dimensional Electron System. *Phys Rev Lett* 97:186404
56. Garcia-Pomar J, Cortijo A, Nieto-Vesperinas M (2008) Fully valley-polarized electron beams in graphene. *Phys Rev Lett* 100:236801
57. Akhmerov AR, Beenakker CWJ (2007) Detection of Valley Polarization in Graphene by a Superconducting Contact. *Phys Rev Lett* 98:157003
58. Wu GY, Lue N-Y, Chang L (2011) Graphene quantum dots for valley-based quantum computing: A feasibility study. *Phys Rev B* 84:195463
59. Conwell EM (1967) *High Field Transport in Semiconductors*. Academic Press
60. Trauernicht DP, Wolfe JP (1986) Drift and diffusion of paraexcitons in Cu₂O: Deformation-potential scattering in the low-temperature regime. *Phys Rev B* 33:8506–8521. doi: 10.1103/PhysRevB.33.8506
61. Nesladek M, Bogdan A, Deferme W, et al (2008) Charge transport in high mobility single crystal diamond. *Diam Relat Mater* 17:1235–1240
62. Erginsoy C (1950) Neutral impurity scattering in semiconductors. *Phys Rev* 79:1013–1014
63. Böer KW (2002) *Survey of Semiconductor Physics*, second ed. John Wiley & Sons, New York
64. Conwell E, Weisskopf VF (1950) Theory of Impurity Scattering in Semiconductors. *Phys Rev* 77:388–390. doi: 10.1103/PhysRev.77.388
65. Suntornwipat N, Gabrysch M, Majdi S, et al (2016) Magnetotransport study of valley-polarized electrons in synthetic diamond. *Phys Rev B* 94:035408. doi: 10.1103/PhysRevB.94.035408
66. Shockley W (1938) Currents to conductors induced by a moving point charge. *J Appl Phys* 9:635–636
67. Ramo S (1939) Currents induced by electron motion. *IRE Proc* 27:584–585
68. Isberg J, Gabrysch M, Tajani A, Twitchen DJ (2006) Transient current electric field profiling of single crystal CVD diamond. *Semicond Sci Technol* 21:1193. doi: 10.1088/0268-1242/21/8/035

Acta Universitatis Upsaliensis

*Digital Comprehensive Summaries of Uppsala Dissertations
from the Faculty of Science and Technology 1670*

Editor: The Dean of the Faculty of Science and Technology

A doctoral dissertation from the Faculty of Science and Technology, Uppsala University, is usually a summary of a number of papers. A few copies of the complete dissertation are kept at major Swedish research libraries, while the summary alone is distributed internationally through the series Digital Comprehensive Summaries of Uppsala Dissertations from the Faculty of Science and Technology. (Prior to January, 2005, the series was published under the title “Comprehensive Summaries of Uppsala Dissertations from the Faculty of Science and Technology”.)

Distribution: publications.uu.se
urn:nbn:se:uu:diva-348551



ACTA
UNIVERSITATIS
UPSALIENSIS
UPPSALA
2018